 

*CONFERENCES AND SYMPOSIA* PACS number: 01.10.Fv

# Scientific session of the Physical Sciences Division of the Russian Academy of Sciences (29 March 2006)

A scientific session of the Physical Sciences Division of the Russian Academy of Sciences (RAS) was held in the Conference Hall of the Lebedev Physics Institute, Russian Academy of Sciences, on 29 March 2006. The following reports were presented at the session:

(1) **Bunkin A F, Nurmatov A A, Pershin S M** (Wave Research Center at the Prokhorov General Physics Institute, RAS, Moscow) "Coherent four-photon spectroscopy of low-frequency molecular librations in a liquid";

(2) **Simonenko V A** (Russian Federal Nuclear Center — Zababakhin All-Russia Scientific Research Institute of Technical Physics, Snezhinsk, Chelyabinsk region) "Nuclear explosions as a probing tool for high-intensity processes and extreme states of matter: some applications of results";

(3) **Buchelnikov V D, Taskaev S V** (Chelyabinsk State University), **Vasiliev A N** (Lomonosov Moscow State University), **Koledov V V, Khovaylo V V, Shavrov V G** (Institute of Radioengineering and Electronics, RAS, Moscow) "Magnetic shape-memory alloys: phase transitions and functional properties."

A brief presentation of the reports is given below.

PACS numbers: **33.20. – t**, **42.65. – k**, 87.50.Jk
DOI: 10.1070/PU2006v049n08ABEH006082

## Coherent four-photon spectroscopy of low-frequency molecular librations in a liquid

A F Bunkin, A A Nurmatov, S M Pershin

### 1. Introduction

One of the most urgent problems in the investigation of associated liquids (including liquid water and aqueous solutions of proteins) is the study of the short-range molecular structure of these media, as well as the shape and dimensions of molecular complexes formed by strong intermolecular interactions. This information may be gained from thermal neutron scattering data [1 – 3] and from the optical spectra of low-frequency molecular motion in liquids. The spectra of spontaneous Raman scattering (RS) (in the range $< 100$ cm$^{-1}$) and Rayleigh-wing scattering [4] in the vicinity of zero frequency detuning also contain information about the structure of molecular complexes in liquids, because they depend on intermolecular vibrations and orientational molecular motion. But the use of classical optical spectroscopic techniques [infrared (IR) absorption and RS] in the spectral range from several to 100 cm$^{-1}$ (0 – 100 THz) runs into several experimental problems.

A separate complicated problem is the spectroscopy of low-frequency vibrational and rotational resonances in the 1 – 5 cm$^{-1}$ range. These resonances arise in the media where stable molecular complexes of complex shape may exist with a lifetime far exceeding the hydrogen bond switching time $\sim 10^{-13}$ s. Such resonances may emerge in biological macromolecules consisting, as a rule, of subglobules with a molecular weight of $\sim 10^3$ atomic units connected by peptide or hydrogen bonds [5, 6]. The study of these resonances deepens the understanding of the geometry of linkage between biological molecules and solvent molecules, as well as the mechanics of motion of these complexes.

One of the areas of nonlinear optics spectroscopy that permits an efficient solution to this problem is the four-photon Rayleigh-wing spectroscopy [7, 8]. This approach allows substantially improving the signal-to-noise ratio in low-frequency spectra by phasing the orientational and translational molecular motion in a macroscopic volume with the aid of two laser waves with frequencies $\omega_1$ and $\omega_2$ whose difference $\omega_1 - \omega_2$ is scanned in the range of the Rayleigh wing. The parameter measured in this case is the state of radiation polarization at the frequency $\omega_s = \omega_1 - (\omega_1 - \omega_2)$, whose nonlinear source is of the form [9, 10]

$$\mathbf{P}_i^{(3)} = 6\chi_{ijkl}^{(3)}(\omega_s; \omega_1; \omega_2; -\omega_1)\mathbf{E}_j^{(1)}\mathbf{E}_k^{(2)}\mathbf{E}_l^{(1)*}, \qquad (1)$$

where $\chi^{(3)}$ is the cubic susceptibility of the medium, which is proportional to the correlation function of optical anisotropy fluctuations, and $\mathbf{E}^{(1)}$ and $\mathbf{E}^{(2)}$ are the amplitudes of the interacting fields. The recorded signal intensity is $I_s \propto \left|\chi^{(3)}\right|^2 I_1^2 I_2$. We emphasize that the four-photon interaction between the laser fields and the ensemble of molecules defines the phase of their vibrational and rotational modes in the entire volume of the medium that is simultaneously exposed to radiation with frequencies $\omega_1$ and $\omega_2$.

The spectral resolution in the four-photon spectroscopy is determined by the width of the instrumental function, which is equal, in the first approximation, to the convolution of the spectral linewidths of both lasers with frequencies $\omega_1$ and $\omega_2$. In our measurements (see Sections 2 and 3), these frequencies were in the transparency range of the medium under investigation; the spectral resolution was equal to $\sim 0.1$ cm$^{-1}$.

We emphasize that in the four-photon Rayleigh-wing spectroscopy, with the proper selection of the polarization of the waves $\mathbf{E}^{(1)}$ and $\mathbf{E}^{(2)}$ [6 – 8], measurements are made of the signal proportional to the imaginary part of the cubic susceptibility of the medium: $I_s \sim \left(\mathrm{Im}\,\chi^{(3)}\right)^2$. This circumstance furnishes a significant advantage of four-photon scattering over IR spectroscopy because it opens up the

*Uspekhi Fizicheskikh Nauk* **176** (8) 883 – 906 (2006)
Translated by E N Ragozin, E G Strel'chenko, S N Gorin; edited by A M Semikhatov

possibility of recording, with the use of a single experimental technique, the resonances of electromagnetic radiation absorption for liquid layers up to 30 cm in thickness in a broad (*up to the terahertz range*) spectral range (0 – 30 THz). Without question, this advantage is fundamentally important in the investigation of biomacromolecules, because it permits studying their low-frequency spectra in the natural medium — in aqueous solutions. Interestingly, completely spanning this frequency range (0 – 30 THz) in millimeter and submillimeter spectroscopy requires using several types of radiation sources [1].

Another advantage consists in the possibility of distinguishing between the contributions to the measured signal arising from different mechanisms of orientational relaxation in liquids [12, 13], which are variously manifested in four-photon scattering spectra. In particular, the line broadening centered at the zero frequency, $\omega_1 - \omega_2 = 0$ (the narrow part of the Rayleigh wing), is due to the slow orientational motion of molecular associates, while the contribution of fast rotational molecular motion must show up in the broad part of the Rayleigh wing, $|\omega_1 - \omega_2| > 1$. Several authors [12, 13] have discussed the possibility that there exists orientational relaxation equivalent to the free rotation of molecules in the liquid phase in a time shorter than 1 ps. But to our knowledge, a spectrum consisting of narrow resonances of free molecular rotation in a liquid has not so far been directly recorded.

One of the basic problems arising in liquid-state physics, in particular in the physics of water, consists in providing an explanation of the special features of the hydrogen bond in media whose molecules differ by the value of the nuclear spin of hydrogen atoms. An example of such molecules is the ortho- and paramodifications of water molecules, in which the total spin of hydrogen is either 1 (orthomolecules) or 0 (paraisomers). The ortho- and paraisomers of $H_2O$ molecules in water vapor are in the ratio 3 : 1 in equilibrium conditions. They differ by the rotational spectrum [14] and are readily identified in the gas phase [15]. It was discovered in [15] that water vapor, when passed through a porous material with a developed surface or above the surface of organic (DNA, lysozyme protein) or inorganic compounds [16], is enriched with orthoisomer molecules. The observed selective deviation from the equilibrium ratio was attributed to the fact that the orthoisomer water molecules have a higher mobility, while the paramolecules are characterized by a greater capacity to form complexes. The question of whether the ortho- and paracomponents of water exist and spectroscopically show up in the liquid phase is still open. Also, it is still unclear whether there is any selectivity in intermolecular interactions in liquids on the basis of ortho- and paramodifications of molecules.

In this report, we review the recent experiments carried out in the Laboratory of Applied Hydrophysics of the Wave Research Center at the Prokhorov General Physics Institute, RAS. In these experiments, with the aid of four-photon scattering, we observed the spectra of low-frequency librations (torsional vibrations) and rotations of molecules in various liquids in the 0 – 3 THz range. The liquids were selected on the basis of the hypothesis that the contribution of rotational resonances to the four-photon scattering signal increases as the intermolecular interaction becomes weaker. Furthermore, a systematic study was made of the four-photon scattering spectra in the 0 – 100 $cm^{-1}$ range in a macroscopic volume of aqueous solutions of the α-chymotrypsin protein. This range was selected because it contains the Mandel'shtam – Brillouin resonances, the Rayleigh wing, and the RS resonances that correspond to the vibrational and orientation motion of molecular protein fragments and the intrinsic low-frequency spectra of the ortho- and para-spin isomers of $H_2O$ molecules in the liquid phase.

## 2. Experiment

Experiments were carried out on the facility described at length elsewhere [17]. Two counterpropagating waves $\mathbf{E}^{(1)}$ and $\mathbf{E}^{(2)}$ with frequencies $\omega_1$ and $\omega_2$ traveled in a cell filled with a liquid. The entrance and exit cell windows were made of fused quartz and had only an insignificant effect on the state of polarization of transmitted radiation. The wave $\mathbf{E}^{(1)}$ (the second harmonic radiation of an Nd:YAG laser operating in a single longitudinal mode, the intensity typically equal to $\sim 60$ MW $cm^{-2}$) was circularly polarized. The frequency-tunable $\mathbf{E}^{(2)}$ wave with the intensity $\sim 10$ MW $cm^{-2}$ was linearly polarized. With the polarization states of the interacting waves selected in this way [9, 10], the nonresonance contribution made by the electron subsystem of the medium to the signal determined by nonlinear source (1) can be substantially suppressed by tuning the polarization selector.

Because the unit polarization vectors of the signal wave at the frequency $\omega_s$ and of the wave $\mathbf{E}^{(2)}$ are noncollinear and their traveling directions coincide, the four-photon scattering signal was selected by a Glan prism. The width of the spectrometer instrumental function ($\sim 0.1$ $cm^{-1}$) and the spectral range (from $-1200$ to 300 $cm^{-1}$) were determined by the output characteristics of a laser utilizing an ethanol solution of 'Coumarin-500' dye. This laser (the $\mathbf{E}^{(2)}$ wave) was pumped by the third harmonic of Nd:YAG-laser radiation and was program-tunable in frequency. For each value of the frequency $\omega_2$, the signal was averaged over 10 – 30 readings; then, the laser frequency was automatically tuned at intervals $\sim 0.119$ $cm^{-1}$. The zero-frequency detuning was referenced as accurate to 0.02 $cm^{-1}$ using the Mandel'shtam – Brillouin resonances, and the subsequent wavelength tuning was verified using the modes of a Fabry – Perot interferometer with a 7 mm base (with the free spectral range equal to $\sim 1.4$ $cm^{-1}$).

Measurements were made in 'Milli-Q' water ($H_2O$), heavy water ($D_2O$), 30% and 5% aqueous solutions of hydrogen peroxide ($H_2O_2$) and α-chymotrypsin (concentrations of 10 and 17 mg $ml^{-1}$), and carbon tetrachloride ($CCl_4$) in the spectral range between $-100$ and 100 $cm^{-1}$. Here, the negative detuning pertains to the scattering signal in the anti-Stokes region. The 'Milli-Q' water (reagent quality, type I, specific resistance 18.2 MΩ cm, residual impurity under 20 μg $l^{-1}$) was produced in the 'Millipore' facility immediately prior to the experiment. The $D_2O$, $H_2O_2$, and $CCl_4$ samples were commercial OSCh (ultrapure) and KhCh (chemically pure) class reagents. Among the above media, the strongest intermolecular interaction due to the hydrogen bond is observed in $H_2O$ and the weakest in $CCl_4$, whose molecules are considered to be spherical tops [18].

## 3. Experimental results

Figure 1 shows the four-photon scattering spectra in the spectral range from $-8$ to 8 $cm^{-1}$ recorded under similar experimental conditions in $CCl_4$, $H_2O$, and the aqueous solution of hydrogen peroxide. Each of the spectra shows a line doublet (indicated by arrows) in the $\pm 0.5$ $cm^{-1}$ spectral range arising from the scattering by acoustic phonons (the Mandel'shtam – Brillouin resonances) and several narrow

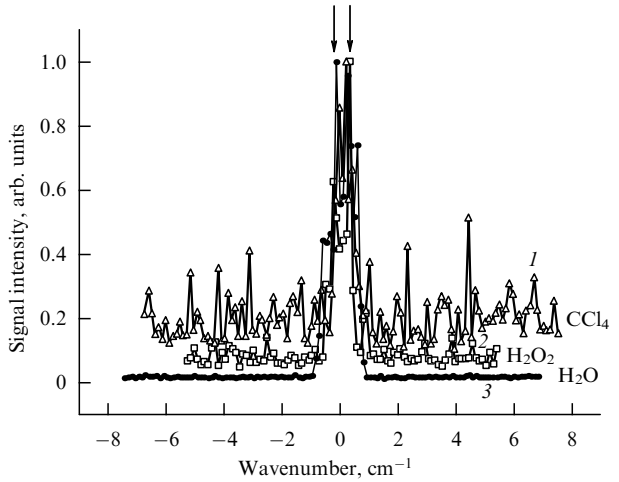


**Figure 1.** Four-photon scattering spectra normalized to the corresponding peaks of the signals due to the Mandel'shtam – Brillouin resonances in the following liquids: $CCl_4$ (curve *1*), $H_2O_2$ (curve *2*), and $H_2O$ (curve *3*) in the spectral range between $-8$ and 8 cm$^{-1}$. In the spectral range $\pm 0.5$ cm$^{-1}$, each of the spectra shows a line doublet (indicated by arrows) arising from the scattering by acoustic phonons.

resonances in the region $> 1$ cm$^{-1}$, which are comparable in width to the spectrometer instrumental function. For convenience of comparison, the spectra plotted in Fig. 1 are normalized to the corresponding peaks of the signals of the four-photon scattering due to the Mandel'shtam – Brillouin resonances, whose cross section in $CCl_4$ is approximately 5 times greater than in water [10]. This circumstance is responsible for the corresponding apparent lowering of resonance amplitudes in $CCl_4$ (see Fig. 1). One can see from the spectra that the greatest contribution to the scattering signal outside the $\pm 1$ cm$^{-1}$ range is in $CCl_4$ and the smallest is in $H_2O$. The increase in the contribution of the narrow resonances to the spectrum of the aqueous solution of $H_2O_2$ in comparison with the contribution of these resonances to the spectrum of water ($H_2O$) is attributable to the weakening of intermolecular interaction in hydrogen peroxide. It is well known that the $H_2O_2$ molecules form two hydrogen bonds with $H_2O$, while the water molecules form four bonds [1, 2].

Figure 2a shows a part of the four-photon scattering spectrum in the region $\omega_1 - \omega_2 > 0$ for liquid $CCl_4$ (curve *1*) on which the part of the same spectrum in the anti-Stokes region $\omega_1 - \omega_2 < 0$ (curve *2*) is superimposed. The frequencies of the rotational spectrum of free $^{12}C^{35}Cl_4$ molecules (the fraction of these molecules in $CCl_4$ is equal to $\sim 32.54\%$ [19]) obtained by *ab initio* calculations are indicated by vertical lines. The calculation was performed neglecting the isotopic substitution of Cl and C atoms [19]. Figure 2a suggests that the spectral positions of the resonances for a positive (curve *1*) and negative (curve *2*) detuning agree satisfactorily (to within the instrumental function) with the calculated ones for the rotational spectrum of the $CCl_4$ gas. Extra lines in the experimental spectrum are supposedly due to the occurrence of resonances of the $CCl_4$ molecules with a different isotopic composition. Approximating the spectrum in Fig. 2a by the function $0.267 \exp\left[(\omega_1 - \omega_2)/0.647\right] + 0.12$, which has the width $\sim 1.3$ cm$^{-1}$ at the level of e$^{-1}$, permits estimating the time of orientational relaxation due to low-frequency molecular librations as $\sim 25$ ps. This value coincides with the characteristic time (10 – 50 ps) of dielectric relaxation of organic liquids [20].

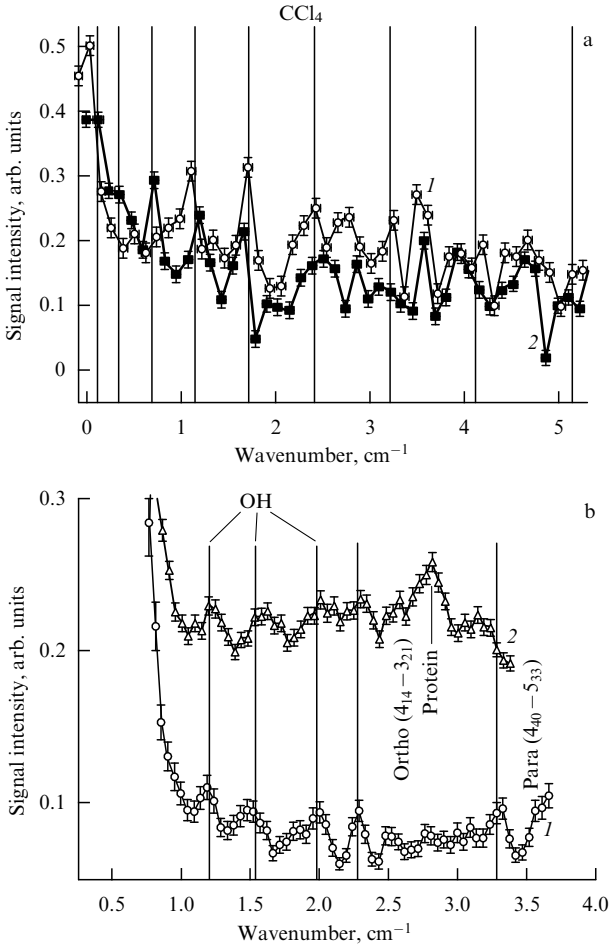


**Figure 2.** (a) Part of the four-photon scattering spectrum in the region $\omega_1 - \omega_2 > 0$ for liquid $CCl_4$ (curve *1*) on which the part of the same spectrum in the region $\omega_1 - \omega_2 < 0$ (curve *2*) is superimposed. The vertical lines indicate the frequencies of the rotational RS spectrum of the $CCl_4$ molecule calculated *ab initio*. (b) Spectra of the four-photon scattering in water (curve *1*) and protein solution (curve *2*). The vertical lines indicate the resonance frequencies of the OH and $H_2O$ molecules.

Figure 2b shows fragments of the spectra of $H_2O$ (curve *1*) and aqueous solution of α-chymotrypsin (curve *2*) at the concentration 10 mg ml$^{-1}$. Water resonances are indicated by vertical lines. The α-chymotrypsin line (2.8 cm$^{-1}$) is labeled. The 2.26 cm$^{-1}$ and 3.21 cm$^{-1}$ water resonances are attributed, with an accuracy of the instrumental function, to the rotational transitions $4_{14} - 3_{21}$ and $5_{33} - 4_{40}$ of the ground vibrational state of the ortho- and para-spin isomers of water molecules, respectively [14]. From spectrum *2* (Fig. 2b), it is clear that the 3.21 cm$^{-1}$ line of the paraisomer of water is absent from the solution of protein. This fact is supposedly due to the selective damping of free rotation and the bonding of water paraisomer molecules by protein molecules, as in the case where the vapor is passed above a rough surface [16].

A series of experiments was conducted in which the four-photon scattering spectrum was recorded under similar conditions in heavy ($D_2O$) and light ($H_2O$) water and their 50% mixture in the 0 – 100 cm$^{-1}$ (0 – 3 THz) range. The aim of these experiments was to compare the rotational resonance frequencies observed for the $D_2O$ and $H_2O$ molecules in the liquid phase with the values tabulated in Refs [14, 21]. As an example, Fig. 3a shows the spectrum of the $H_2O - D_2O$ mixture (1 : 1) in the 0 – 50 cm$^{-1}$ range smoothed over three

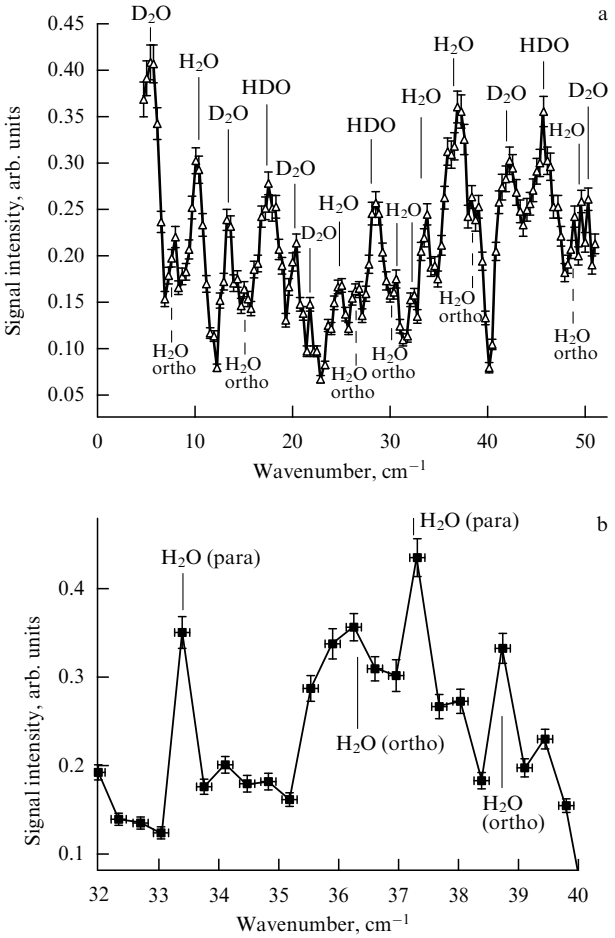


**Figure 3.** (a) Four-photon scattering spectrum in the 50 : 50 mixture of heavy ($D_2O$) and light ($H_2O$) water. (b) Fragment of the spectrum shown in Fig. 3a in the region of the 36.6 and 37.13 cm$^{-1}$ line doublet arising from transitions in the ortho- and para-spin isomers of water molecules.

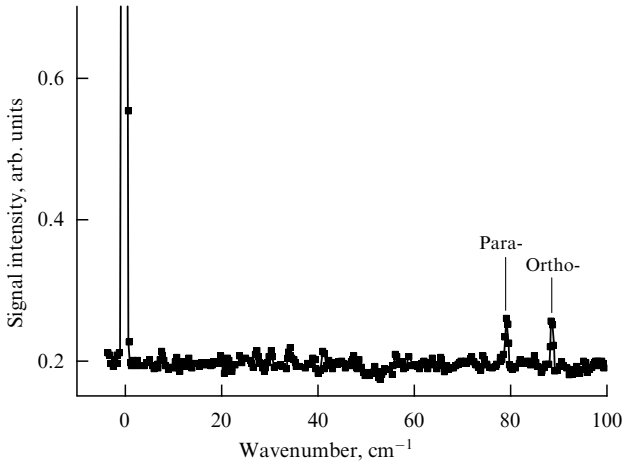


**Figure 4.** Panoramic four-photon scattering spectrum in 'Milli-Q' water in the 0 – 100 cm$^{-1}$ range.

experimental points to simplify the comparison with the tabular data. The rotational transition resonances pertaining, according to the data in Refs [14, 21, 22], to the spectra of free rotation of the $D_2O$, $H_2O$, and HDO molecules, are indicated by labels. The dashed indications pertain to the most intense lines of the rotational transitions of the water ortho-spin isomer. Figure 3b gives the 32 – 40 cm$^{-1}$ portion of the spectrum, where four lines of the ortho- and paramolecules of $H_2O$ show up [14]. Interestingly, the ratio between the line amplitudes in these spectra may differ from their ratio in the IR absorption spectrum because in the four-photon scattering they are proportional to $(1 - 3\rho)$, where $\rho$ is the degree of depolarization of the corresponding RS-active resonances [10]. It is pertinent to note that the rotational resonances of the three types of molecules ($D_2O$, $H_2O$, and HDO) are observed in the four-photon scattering spectra of the 50% liquid $D_2O - H_2O$ mixture without noticeable frequency shifts.

The last-mentioned circumstance calls for elucidation. The issue of the effect of intermolecular interaction on the RS and IR absorption resonance frequency shifts in transforming from a gas to a liquid was intensively investigated in the middle of the 20th century (see, e.g., monograph [23]). For different interaction types, this shift was shown to range from $\sim 0.2\%$ to $\sim 0.001\%$ of the corresponding transition frequencies. Clearly, for molecular vibration frequencies, which lie in the 1000 – 4000 cm$^{-1}$ range, this correction is appreciable in magnitude. But for the rotational resonances in the $< 100$ cm$^{-1}$ region observed in our experiments, this shift should be of the order of 0.2 cm$^{-1}$, i.e., comparable to the width of the spectrometer instrumental function.

A series of experiments was conducted to reveal the effect of protein molecules on the ortho- and para-spin isomers of a molecule in the liquid phase. Figure 4 shows the spectrum of deionized 'Milli-Q' water in the 0 – 100 cm$^{-1}$ range. The 79.8 cm$^{-1}$ (paramolecule) and 88.1 cm$^{-1}$ (orthomolecule) resonances [14, 24], the strongest in the above range, are clearly visible in the spectrum and are indicated by the corresponding labels. These resonances pertain to the $(4_{04} - 3_{13})$ and $(4_{14} - 3_{03})$ rotational transitions of the ground vibrational state of the para- and ortho-spin isomers of water molecules, respectively. Specified in parentheses are the rotational quantum numbers $J$, $K_a$, and $K_c$ of the initial and final levels for the corresponding transitions of the main water isotope borrowed from the HITRAN (high-resolution transmission molecular absorption) database [14]. We emphasize that the majority of the rest lines of the water vapor absorption spectrum in the 0 – 100 cm$^{-1}$ range are formed by superposition of close resonances of the ortho- and paraisomers of water [14] and are therefore less suitable for solving the problem formulated above.

Figure 5 shows the fragment of the water spectrum in the 73 – 91 cm$^{-1}$ frequency detuning range. Using the HITRAN database [14], all resonances observed in the spectrum can be ascribed to the rotational transitions of the lower vibrational state 74.1 cm$^{-1}$ $(5_{14} - 5_{05})$, 78.2 cm$^{-1}$ $(7_{25} - 7_{16})$, and 88.1 cm$^{-1}$ $(4_{14} - 3_{03})$ of orthomodifications and 79.8 cm$^{-1}$ $(4_{04} - 3_{13})$, 85.0 cm$^{-1}$ $(9_{46} - 8_{53})$, and 90.8 cm$^{-1}$ $(12_{75} - 11_{84})$ of paramodifications of the main isotope of the $H_2O$ molecule. The resonances of ortho- and paramolecules of water are indicated.

Figure 6 shows the fragments of the spectra of the $\alpha$-chymotrypsin protein solution (for the concentration 17 mg ml$^{-1}$) and the 'Milli-Q' water in the 73 – 91 cm$^{-1}$ range. For convenience of comparison, the water spectrum is extended eight-fold along the vertical axis. The rotational resonances of the ortho- and paraisomers of the water molecule are indicated respectively by thin and bold arrows. These resonances were ascribed to the frequencies using the data in Ref. [14]. The following rotational transitions of the

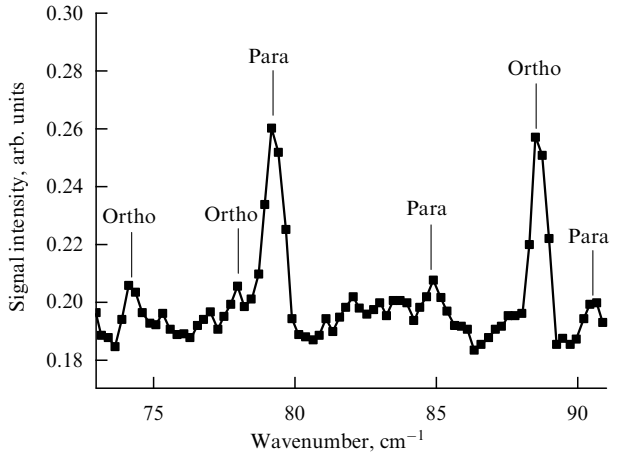


**Figure 5.** Fragment of the 'Milli-Q' water spectrum in the 73–91 cm$^{-1}$ frequency detuning range. Indicated are the resonances of ortho- and paramolecules of $H_2O$.

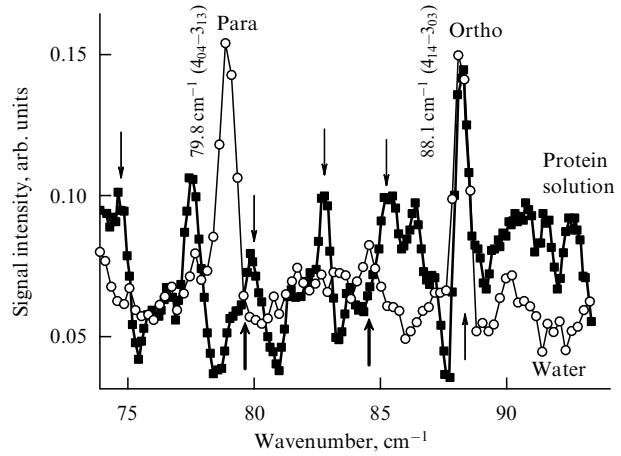


**Figure 6.** Fragments of the spectra of an aqueous solution of α-chymotrypsin (for the concentration 17 mg ml$^{-1}$) and 'Milli-Q' water in the 73–91 cm$^{-1}$ range. The rotational resonances of ortho- and paraisomers of the molecule are indicated respectively by thin and bold arrows.

orthomodification of water are clearly identified in Fig. 6: 73.3 cm$^{-1}$ ($3_{30}-3_{21}$), 74.1 cm$^{-1}$ ($5_{14}-5_{05}$), 77.3 cm$^{-1}$ ($9_{45}-9_{36}$), 81.0 cm$^{-1}$ ($9_{36}-9_{27}$), 82.15 cm$^{-1}$ ($4_{32}-4_{23}$), 83.5 cm$^{-1}$ ($10_{47}-9_{54}$), 85.6 cm$^{-1}$ ($7_{34}-7_{25}$), 86.4 cm$^{-1}$ ($4_{23}-4_{14}$), and 88.1 cm$^{-1}$ ($4_{14}-3_{03}$). We note that the 88.1 cm$^{-1}$ ($4_{14}-3_{03}$) line of the orthoisomer remained dominant in the spectrum upon dissolving α-chymotrypsin in the water, while the 79.8 cm$^{-1}$ ($4_{04}-3_{13}$) line of the paraisomer turned out to be strongly suppressed, which points to the selectivity of the interaction of protein molecules with the ortho- and paraisomers of $H_2O$.

## 4. Discussion

The experiments conducted in our work show that the spectra of four-photon laser radiation scattering in several liquids ($CCl_4$, $H_2O$, $D_2O$, $H_2O_2$) exhibit narrow resonances, which coincide in frequency, to within the width of the spectrometer instrumental function, with the rotational transitions of the ground electronic and vibrational states of the corresponding molecules. In this case, separately identified in the spectrum of liquid water are the lines pertaining to orthomodifications and paramodifications of the main isotope of the $H_2O$ molecule. The same lines are observed to be almost ten times stronger in the spectra of the aqueous solution of α-chymotrypsin. This fact testifies to the increase in the fraction of free water molecules in the protein solution.

The increase in the rotational spectrum contribution to the signal of four-photon scattering in the protein solution in comparison with the similar contribution in the case of $H_2O$ is attributable to the formation of a weak hydrogen bond between the water and protein molecules. The experimentally observed suppression of the rotational lines chiefly of the paraisomer of water molecules in the protein solution indicates the selective hydration of biological macromolecules by the paraisomers of water molecules. We note that the selective sorption from the gas phase of the paraisomers of water molecules in passing above the surface of DNA, lysozyme, and collagen samples was previously observed in Ref. [25].

Arguably, the free motion of molecules in liquids emerges at the instant the force of intermolecular interaction (which is strongest in water due to the hydrogen bond) vanishes for some molecules as a result of density fluctuations in the thermal molecular motion. This force rapidly changes with the intermolecular distance because, for instance, for the Lenard-Jones potential

$$U(r) = -\frac{a}{r^6} + \frac{b}{r^{12}}, \qquad (2)$$

the attractive force decreases as $\sim r^{-7}$. As a result, individual molecules acquire the capacity for free motion, to essentially become gas molecules.

The existence of a rotational structure in four-photon scattering spectra enables one to spectrally separate the fast and slow motion of molecules and estimate the relative fraction of their contributions. This possibility is nonexistent in RS and nuclear magnetic resonance, where all kinds of orientational motion make contributions to the broadening of the resonances recorded [3, 4, 12, 13]. The spectra of liquids obtained in our experiments are indicative of an appreciable number of free molecules that do not participate in the formation of associated complexes at the instant of probing.

Because every resonance whose contribution to the four-photon spectrum is proportional to $(\mathrm{Im}\,\chi^{(3)})^2$ [see relation (1)] is reflective of some mechanism of energy dissipation in the medium (hypersonic waves, librations, free molecular motion), the curves in Figs 1–6 reproduce the absorption spectra of the media under investigation in the terahertz and subterahertz frequency ranges. The fact that these spectra are not continuous permits finding the frequencies at which different liquids, in particular water, exhibit a higher or lower level of microwave radiation absorption. This circumstance allows reconsidering the numerous facts surrounding the selective action of microwave radiation on living organisms [11]. In this case, the high $Q$ value of resonances with a linewidth no greater than the width of the instrumental function ($\sim 0.2$ cm$^{-1}$) suggests the feasibility of their saturation under pulsed exposure to resonance radiation. The spectral separation of the contribution of slow and fast motion to the orientational molecular relaxation opens up additional possibilities for the study of molecular interactions in the physics of liquids [26].

It is beyond the scope of this report to discuss the results of a series of works on the measurement of the fractal dimension

of polymers, molecular associates, and biological macromolecules in a liquid using four-photon low-frequency scattering spectra. Rapid strides are being made in this area [27, 28]. In our experiments [29, 30], a study was made of the spectral response of coherent four-photon laser-radiation Rayleigh-wing scattering, which was used to calculate the phonon state density dispersion. The phonon state density dispersion is known [27, 28] to be the main source of information in the study of the fractal dimensionality of condensed media. We have elaborated an approach offering several advantages over traditional techniques of low-angle scattering of thermal neutrons and X-rays, as well as over spontaneous Rayleigh-wing scattering of light. These advantages include the relative simplicity of the experiment; a high level of the desired signal in comparison with the signal level in the case of spontaneous Rayleigh-wing scattering; a high energy (spectral) resolution, especially in comparison with the resolution in neutron diffraction analysis; and the possibility, due to the coherent nature of the scattering, of extracting the components arising from the slow reorientations of large molecular fragments in the recorded signal. We emphasize that the last-mentioned factor is nonexistent in the traditional approaches to the measurement of the fractal dimension.

Of special interest is the successful recording of low-frequency spectra of aqueous solutions of proteins in water, i.e., in the medium natural for biological molecules. It is noteworthy that the solution of the α-chymotrypsin protein was accompanied by the manifestation of the selective property to form complexes only with the paraisomer of water molecules. Recording the capacity for spin-selective adsorption of proteins in an aqueous solution allows developing radically new approaches to the investigation of the properties of the membrane aquaporin protein, which is responsible for the transmission of a consecutive chain of single water molecules into a cell. Its discovery was rewarded with a Nobel Prize [31].

The practical significance of the low-frequency resonances discovered in water is evident. Undoubtedly, the most interesting in this case is the study of the influence of microwave radiation and the means of mobile communication with the frequency $\sim 1.8$ GHz on biological subjects. This stems from the fact that water and hydroxyl molecules have rotational resonances at the frequencies 0.072 $cm^{-1}$ (2.16 GHz) and 0.057 $cm^{-1}$ (1.72 GHz), which are close to the frequencies of microwave devices and the radiation of space masers utilizing these molecules [32].

## 5. Conclusion

For the first time, with the aid of coherent four-photon scattering, it has been possible to discover narrow resonances in several liquids ($CCl_4$, $H_2O$, $D_2O$, $H_2O_2$) in the submillimeter wavelength range. These resonances coincide in frequency, to within the width of the spectrometer instrumental function, with the rotational transitions of the ground electronic and vibrational states of the corresponding molecules. The water spectra clearly exhibit resonances pertaining to the lines of the ortho- and paraisomers of the main isotope of $H_2O$ molecules in the gas phase.

The resonance contribution of coherent librations to the four-photon scattering signal significantly increases in passing from water to a protein solution. The mechanism of this effect is not yet completely clear. However, it is conceivable that the presence of protein molecules in the solution is responsible for the disruption of the initial topology of the hydrogen bond network in water, increasing the concentration of weakly bound molecules.

The protein molecule in solution was found to actively interact with the paramodification of the $H_2O$ molecule. This effect permits interpreting the selectivity of microwave radiation action on biological subjects [11] and offers prospects for developing a new class of laser biotechnologies.

**Acknowledgements.** This work was supported in part by the Russian Foundation for Basic Research (Grant Nos 05-02-16020, 05-02-08311), the Optical Spectroscopy and Frequency Standards Program of the Russian Academy of Sciences, and Grant No. 1553.2003 from the Program for the Support of Scientific Schools of the Russian Federation.

## References

1. Eisenberg D, Kauzmann W *The Structure and Properties of Water* (New York: Oxford Univ. Press, 1969)
2. Walley E, in *The Hydrogen Bond*: *Recent Developments in Theory and Experiments* (Eds P Schuster, G Zundel, C Sandorfy) (Amsterdam: North-Holland, 1976) Ch. 29
3. Okhulkov A V, Demianets Yu N, Gorbaty Yu E *J. Chem. Phys.* **100** 1578 (1994)
4. De Santis A et al. *Chem. Phys. Lett.* **133** 381 (1987)
5. Brown K G et al. *Proc. Natl. Acad. Sci. USA* **69** 1467 (1972)
6. Genzel L et al. *Biopolymers* **15** 219 (1976)
7. Bunkin A F et al. *Phys. Rev. B* **52** 9360 (1995)
8. Bunkin A F et al. *J. Raman Spectrosc.* **36** 145 (2005)
9. Shen Y R *The Principles of Nonlinear Optics* (New York: J. Wiley, 1984) [Translated into Russian (Moscow: Nauka, 1989)]
10. Akhmanov S A, Koroteev N I *Metody Nelineinoi Optiki v Spektroskopii Rasseyaniya Sveta*: *Aktivnaya Spektroskopiya Rasseyaniya Sveta* (Nonlinear Optical Methods in Light Scattering Spectroscopy: Active Light Scattering Spectroscopy) (Moscow: Nauka, 1981)
11. Betskii O V, Devyatkov N D, Kislov V V *Biomeditsinskaya Radioelektron.* (4) 13 (1998)
12. Bartoli F J, Litovitz T A *J. Chem. Phys.* **56** 413 (1972)
13. O'Reilly D E, Peterson E M, Scheie C E *J. Chem. Phys.* **60** 1603 (1974)
14. Rothman L S et al. *J. Quant. Spectrosc. Radiat. Transf.* **96** 139 (2005); http://www.elsevier.com/locate/jqsrt
15. Oka T, in *Advances in Atomic and Molecular Physics* Vol. 9 (Ed. D R Bates) (New York: Academic Press, 1973) p. 127
16. Tikhonov V I, Volkov A A *Science* **296** 2363 (2002)
17. Bunkin A F, Nurmatov A A *Laser Phys.* **13** 328 (2003)
18. Weber A (Ed.) *Raman Spectroscopy of Gases and Liquids* (Berlin: Springer-Verlag, 1979)
19. Tse W S, Lin S J *Chinese J. Phys.* **25** 581 (1987)
20. Vuks M F *Elektricheskie i Opticheskie Svoistva Molekul i Kondensirovannykh Sred* (Electrical and Optical Properties of Molecules and Condensed Media) (Leningrad: Izd. LGU, 1984)
21. Molecular Spectroscopy, Jet Propulsion Laboratory, California Institute of Technology, http://spec.jpl.nasa.gov
22. Bykov A D, Sinitsa L N, Starikov V I *Eksperimental'nye i Teoreticheskie Metody v Spektroskopii Molekul Vodyanogo Para* (Experimental and Theoretical Methods in Spectroscopy of Water Vapor Molecules) (Novosibirsk: Izd. SO RAN, 1999)
23. Vol'kenshtein M V, El'yashevich M A, Stepanov B I *Kolebaniya Molekul* (Molecular Vibrations) Vol. 2 (Moscow: GITTL, 1949)
24. Avila G et al. *J. Mol. Spectrosc.* **220** 259 (2003)
25. Potekhin S A, Khusainova R S *Biophys. Chem.* **118** 84 (2005)
26. Gaiduk V I, Gaiduk V V, McConnell J *Physica A* **222** 46 (1995)
27. Pietronero L, Tosatti E (Eds) *Fractals in Physics*: *Proc. of the Sixth Trieste Intern. Symp., Trieste, Italy, July 9–12, 1985* (Amsterdam: North-Holland, 1986)
28. Alexander S *Phys. Rev. B* **40** 7953 (1989)
29. Bunkin A F et al. *Laser Phys.* **15** 707 (2005)

30. Bunkin A F et al. *J. Raman Spectrosc.* **37** 693 (2006)
31. Murata K et al. *Nature* **407** 599 (2000)
32. Strel'nitskiĭ V S *Usp. Fiz. Nauk* **113** 463 (1974) [*Sov. Phys. Usp.* **17** 507 (1975)]

PACS numbers: **28.70.+y**, **62.50.+p**, 97.80.Jp
DOI: 10.1070/PU2006v049n08ABEH006080

# Nuclear explosions as a probing tool for high-intensity processes and extreme states of matter: some applications of results

V A Simonenko

## 1. Introduction

Nuclear explosions, along with releasing massive amounts of energy, involve high initial density and intense fluxes of neutron, gamma, X-ray, and electromagnetic radiation, as well as intense radiation, fluid dynamic, electromagnetic, and seismic processes — all this providing a way to study phenomena previously beyond our reach. One example is the self-similarity property of the shock wave flow [1–3] — an important feature of the evolution of high-power explosions in gases, which was already discovered when the first air nuclear explosions were being prepared and carried out and which was later observed and used in laboratory experiments (for example, in the energy diagnostics of high-intensity laser pulses [4]) and in interpreting explosion phenomena in astrophysics.

For explosions of a sufficiently high intensity, assuming a power-law temperature dependence of the heat conductivity, the self-similarity property is also found at an earlier, thermal stage of energy transfer [5, 6]. Such processes occur when radiation and matter have already thermalized but gas-dynamic energy transfer is still negligibly small. The modes of behavior at this stage also carry information about the nonlinear heat conduction properties of the matter involved. Preceding the thermal stage is that of the nonequilibrium propagation of radiation (which was analyzed in [7] for air explosions). The explosion evolution in the air involves a number of gasdynamic, thermal, and optical processes (see monograph [6] for a review), many of which were invoked to justify and apply the methods with which the energy of air explosions was measured.

In Russia, the transition to underground explosions in 1964 posed new problems but also improved opportunities for physical research in the field. Although they share some similar stages with their air counterparts, underground explosions are different in both scale and the underlying physics.

During the period of air tests, only one on-site experiment — the physics experiment of 1957 — was successfully carried out using high-intensity processes for research purposes [8]. With underground explosions, a similar research was begun in our institute in the first on-site experiments and continued until the last test in 1989. The present author has been privileged to have participated in setting up, performing, and interpreting most of these experiments.

This research stimulated efforts to develop theoretical models and mathematical software tools for describing extreme states of matter and high-intensity pulsed processes — work that was paralleled by special-purpose on-site experiments designed to test models and their mathematical realization and to accumulate experimental data. In this way, a science technology including theoretical work, mathematical simulation, and associated experimentation tools and facilities was developed and subsequently further improved, adapted, and applied to new classes of phenomena, such as the interaction of high-power laser beams with matter, the acoustic collapse of microbubbles, high-intensity magnetohydrodynamic processes, and explosion phenomena in astrophysics.

In this talk, the use of explosions as a tool for exploring high-intensity processes and probing the properties of the media involved are briefly described, together with advances in developing theoretical models, and two examples are given to show how other fields can profit from the science technology developed. The first example presents some results on how the threat of small bodies from space (asteroids or comets) hitting Earth can be prevented by using explosions to change their trajectories or to disperse them. The second example discusses a mechanism that governs the propagation of a burning wave on the surface of an accreting neutron star and explains the front modulation of first-type X-ray bursts in low-mass binary systems.

## 2. General characteristics of explosions and the methodology for their study

The most important features of nuclear explosions are that they are highly localized (typically within dozens of centimeters to several meters) and release huge amounts of energy at a very fast rate (time scale ranging from a few nanoseconds to fractions of a millisecond), with the mass of energy-releasing regions ranging from a few to hundreds of kilograms. The amount of energy released in a nuclear reaction can be larger than $\sim 1$ MeV per nucleon. Although the energy density averaged over the masses of the energy-releasing regions is lower than that, the matter can reach the temperature 10 keV or more as the energy of the reaction products is transferred to the surrounding atoms. The total explosion energy $E_0$ varies widely, from fractions of a kiloton to several megatons TNT equivalent ($1\ \text{kt} = 4.18 \times 10^{12}$ J). Because of the high initial temperature, the transfer of the released energy into the surrounding medium first occurs due to radiation. In parallel with this, nonequilibrium neutron and gamma-ray transfer processes operate, which can hinder but can also facilitate doing experiments of high informative value. We note that despite the high energy release density, the energy-releasing regions and the explosive device and its operation supporting system have finite sizes, often comparable to the linear scale of the processes under study (or in use) and must therefore be taken into account in describing the phenomenon.

Underground explosions were carried out in horizontal galleries and vertical holes (see, e.g., Ref. [9]), the burial depth of the charge varying from hundreds of meters to several kilometers, and a specially developed technology ensured the radiation and seismic safety of the experiment. The measurement program was varied on an experiment-to-experiment basis. A special concern was that the conditions at the location of the charge be optimized for conducting the study. While the horizontal scenario is more convenient in this respect, it involves constructing underground workings, drilling holes for instruments, mounting detectors, and

deploying measurement systems and communication channels, which increases the expense. With hole experiments, measurement opportunities were comparatively more limited. In this case, only a limited volume of main holes or, occasionally, of narrow instrument ones was available for mounting the equipment. Experimental setups were assembled on the ground before being lowered to the detonation position together with the explosive device.

In terms of methodology, the following major components can be identified in the study of underground explosions. For the major processes involved, new physical models were developed or already existing ones were used. Often, a complex problem was broken into stages. Based on such models, systems of equations were determined to describe both individual processes and the phenomenon as a whole, and possible initial and boundary conditions were chosen, thus providing standard input data for developing numerical solution algorithms and the corresponding software (with a view to using high computational power). A key aspect of the program was the accumulation of theoretical and experimental data and of software tools for their processing, systematization, and use. Paralleling this were improvements in the relevant physical and mathematical models and programs describing the major processes observed in the tests.

Simultaneously, benchmark experiments were conducted on-site to test the models used, to gather more data, and, ultimately, to justify and further develop the research technology, with the experimental design usually chosen to create as favorable conditions as possible for carrying out specific experimental programs. In many cases, in the preparation of a benchmark experiment, additional experimental research — either in laboratory or as a spinoff of other on-site explosions — was conducted. For all experiments, sufficient computational and theoretical support was provided. Often, benchmark experiments themselves served as preparatory stages for the next generation of experiments.

## 3. Radiation stage of an explosion

As noted in Section 2, at the early stage of a nuclear explosion, the high-rate high-density energy release from it results in energy transfer by hard (X-ray) electromagnetic radiation even in a dense condensed medium. In this process, the following successive phases are distinguished. The first phase is that of spectral transfer. Next, radiation and matter come to equilibrium with one another and radiative heat conduction dominates. In this phase, the front of the heat wave is bordered by a small region in which, even though spectral transfer still exists, it has no effect on the dynamics of the process. For regions close to the center, there exists a time interval during which radiation energy dominates over that of matter.

For sufficiently high values of the explosion energy, the phase of nonlinear radiative heat transfer may be the longest-lasting one in the list, and it is therefore worthwhile discussing it in some more detail. For explosions as powerful as this, it can be considered that energy is released instantaneously at a point. A further assumption of a power-law dependence of the heat conductivity on the temperature allows the self-similar solution to be used in making the estimates [5].

Early theoretical calculations of the nonlinear heat conductivity (specifically, for astrophysical purposes) used the Rosseland procedure (see, e.g., Ref. [6]) to obtain the average radiation length. While astrophysical media are typically dominated by Compton scattering and bremsstrahlung processes, the analysis of nuclear explosion processes strongly suggested that bound-bound transitions should be taken into account, an understanding which to a large extent came due to the on-site experiment of 1957 [8]. As a result, sufficiently accurate quantum-statistical models were developed for predicting the Rosseland mean free path [10]. By the time of the first underground explosions, a regular supply of this kind of data was established. The 1983 special-purpose experiment [8] highlighted the need for further work to improve the theoretical models used. Although the Rosseland mean free path depends on the temperature nonmonotonically in general, the power-law assumption is quite suitable for purposes of estimation.

With these aspects in mind, we return to considering the heat wave. As the wave propagates, its intensity decreases and its front slows down, and at certain distances acoustic perturbations, due to the temperature gradient and inhomogeneities present in the core regions, start to catch up with the front, resulting in the shock front formation and a change from the thermal (T) to the gasdynamic (G) mechanism of energy transfer. Based on the self-similar solution of the heat conduction problem and equating the heat wave velocity to the speed of sound to define the regime changeover, the characteristic linear scale $r_{\mathrm{T}\to\mathrm{G}}$ for the changeover is found to be

$$r_{\mathrm{T}\to\mathrm{G}} = b(n,\gamma)\left(\frac{\varkappa_0^2 E_0^{2n-1}}{B^{2(n+1)}\rho_0^{2n+2m+1}}\right)^{1/(6n-1)}.$$

Here, it is assumed that the matter obeys the ideal gas equation of state $P = B\rho T$; the Rosseland mean free path is $l = l_0 T^{n-3}/\rho^m$; the constant in the nonlinear heat conductivity coefficient is $\varkappa_0 = 4l_0 ca/3$; $c$ is the speed of light; and $a$ is the constant in the expression for the thermal radiation energy density, $\varepsilon_{\mathrm{th\,r}} = aT^4$. The dimensionless factor $b(n,\gamma)$ depends on the dimensionless parameters $n$ and $\gamma$. For rock materials, the characteristic scale is typically $r_{\mathrm{T}\to\mathrm{G}}\,[\mathrm{cm}] \sim 20\big(E\,[\mathrm{kt}]\big)^{0.315}$. As is shown in what follows, it turns out to be compatible with the characteristic size of the gasdynamic motion region at the explosion (see the table). Therefore, viewed from the gasdynamic standpoint, high-power explosions in dense media cannot be considered pointlike.

We recall that for real media, the radiation mean free path depends on temperature in a much more complicated way. In central regions, the radiation energy density may exceed that of matter, suggesting that numerical simulation is needed to obtain a more rigorous description of these processes. Figure 1 presents model calculation results showing the evolution of the heat conduction stage and its transition to the gasdynamic stage for an instantaneous point-like explosion of 100 kt in quartz-containing rock of the initial density 2.65 $\mathrm{cm}^{-3}$. Panel (a) shows the temperature profile evolution. It is seen that at temperatures $T \sim 3-2.5$ keV, the heat wave changes its profile shapes from originally gentle to steeper, stepwise ones, the result of the effective heat conductivity changing at the transition from the radiation-energy- to matter-energy-dominated states. At temperatures $T \sim 1.5$ keV, the shock wave starts to form, as is clearly seen in panel (b) of Fig. 1, which shows density profiles at different times. It may be considered that the shock wave is completely formed by the time the front arrives at the radius $\sim 65$ cm. This is less than the estimates obtained from the above formula (see the table) because the wave changes its law

**Table**

| Parameter / Medium | High-phase density $\rho_0$, g cm$^{-3}$ | Initial density $\rho_{00}$, g cm$^{-3}$ | Speed of sound $c_0$, km s$^{-1}$ | Dynamic radius $r_d$, m kt$^{-1/3}$ | Regime changeover radius $r_{T\to G}$, m for $E_0 = 1$ kt |
|---|---|---|---|---|---|
| Air | | $1.3 \times 10^{-3}$ | 0.365 | 289 | 4.7 |
| Water | 1 | 1 | 1.5 | 12.3 | 0.34 |
| Rock salt | 2.16 | 2.16 | 3.9 | 5.03 | |
| Quartzite | 4.21 | 2.65 | 9.15 | 2.28 | $\sim 0.19$ |
| Granite | 3.64 | 2.56 | 6.33 | 3.06 | $\sim 0.17$ |
| Dolomite | 2.84 | 2.84 | 5.25 | 3.63 | $\sim 0.18$ |
| Aluminum | 2.7 | 2.7 | 5.20 | 3.85 | $\sim 0.14$ |
| Iron | 7.85 | 7.85 | 3.80 | 3.33 | $\sim 0.11$ |

of motion at an earlier stage of the explosion, as was noted above.

In many cases, the finite dimensions of an explosive system, $r_{NE}$, and the size $r_{Ng}$ of the inhomogeneities introduced during the preparation of the experiment are comparable to or even greater than $r_{T\to G}$, further emphasizing the need for numerical calculations. For research purposes (for example, in shock compressibility or opacity studies), 'flat' or 'cylinder' symmetric arrangements were found to be more convenient to arrange. Such experiments used very different installation configurations from possible simplified one-dimensional schemes, making real processes quite difficult to describe. To check the validity of such processes, additional theoretical models and experimental data were used.

The principal results of the study of the early stage of high-energy explosions were that (1) the conditions to optimally ensure the predicted development of processes at the gasdynamic stage were selected; (2) the best suited experimental settings for measuring nonlinear heat conduction properties and ultrahigh compressibility in the heat wave bordering region were selected; (3) new measuring techniques were developed; and (4) major explosion characteristics were measured.

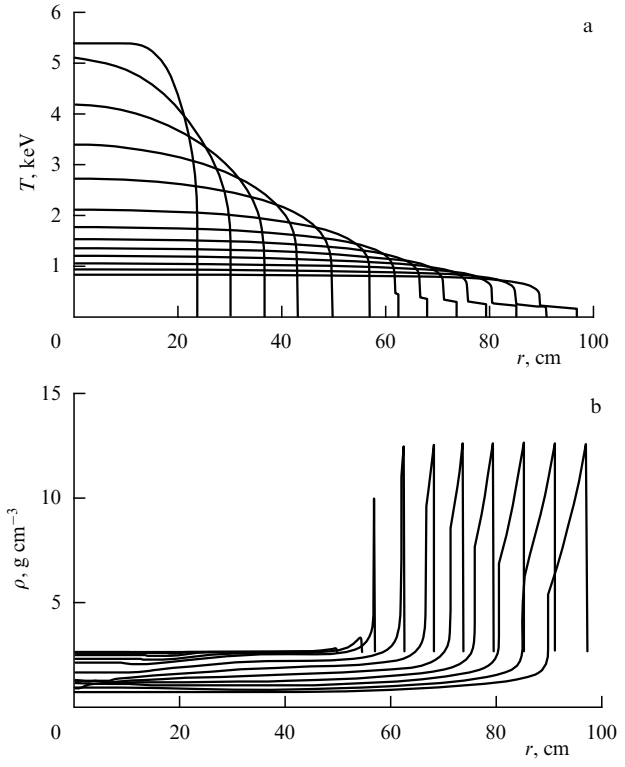


**Figure 1.** The temperature (a) and density (b) profile evolution for a model explosion with $E_0 = 100$ kt in a quartz-containing medium with $\rho_0 = 2.65$ g cm$^{-3}$.

## 4. Gasdynamic stage of an explosion

The change of energy transfer regime primarily shows up in a shock wave starting to form ahead of the heat wave front, whose intensity is subsequently maintained by the energy transfer from the expanding hot matter to cold matter in the region of adiabatic motion. Furthermore, from this point on, the hot matter itself is adiabatically unloaded as it expands. In dense media, the shock-front pressure can reach values of several hundred terapascal (a terapascal is a billion pascals). As the wave propagates, its intensity decreases, and at a sufficiently large distance from the center, the wave front speed $D$ starts approaching a certain effective speed of sound in the medium, $c_0$, which can be regarded as the limit value for the speed of bulk waves. Closer than this, condensed media behave as compressible matters, for which reason this stage is frequently referred to as gasdynamic, and dense medium compressing explosions, as strong.

For an explosion of energy $E_0$ in a medium of the initial density $\rho_0$ and the effective speed of sound $c_0$, the linear scale of the region of gasdynamic motion is the quantity $r_d = (E_0/\rho_0 c_0^2)^{1/3}$, often referred to as the dynamic explosion radius, and the time scale can be taken to be $\tau_d = r_d/c_0$. The time scale for the heat stage is much shorter than $\tau_d$, and therefore, if matter in the inhomogeneity production region has enhanced heat conduction properties (due to poorly filled cavities, for example), then the explosion energy can be considered to be released instantaneously in a certain effective (energy-release) region whose scale $r_E$ is equal to $r_{T\to G}$ or $r_{Ng}$, whichever is larger. This makes calculations for the gasdynamic stage easier in some cases. In more complex cases, however, an accurate description of gasdynamic processes requires that the major inhomogeneities created in carrying out experiments should even be taken into account at the early stages of the phenomenon.

For a sufficiency large region of gasdynamic motion to form in the surrounding medium, the scale $r_E$ must be much smaller than $r_d$. The above arguments apply equally to gaseous and condensed media; however, although the dynamic radius $r_d$ is formally defined in the same way for gases and dense media, there is a fundamental difference between them that influences how the processes involved occur. For condensed media, at not very high temperatures characteristic of the adiabatic stage of the explosion, equations of state (i.e., the dependence of the pressure $P$ and internal energy $\varepsilon$ on the density and temperature) can be

written as a sum of cold (c) terms (due to the elastic interaction of atoms) and thermal terms,

$$P = P_c(\rho) + P_T(\rho, T)\,, \qquad \varepsilon = \varepsilon_c(\rho) + \varepsilon_T(\rho, T)\,.$$

Equations of state for gaseous media contain no cold terms, the quantity $c_0$ is determined only by thermal motions, and the product $\rho_0 c_0^2$ is, up to a constant of the order of unity, the initial thermal pressure. Importantly, the deviation from self-similarity is due to the effect of the initial pressure of the gas ahead of the wave front. In condensed media, the value of $c_0$ is determined by quantum mechanical interactions, the density of matter is significantly larger than in gases, and the product $\rho_0 c_0^2$ greatly exceeds the initial static pressure. The dynamic explosion radius in dense media can be dozens or even hundreds of times smaller than that in gaseous media (see the table). The initial ahead-of-the-wave-front pressure can still be left out of account, and the deviation of the self-similar solution is determined by the presence of 'nonideal' terms in the equation of state. For explosions in dense media, the condition that the scale $r_E$ is smaller than $r_d$ becomes a more acute problem. Indeed, because this condition cannot be satisfied for some values of the explosion energy, special measures were taken to decrease $r_E$ when preparing experiments to study gasdynamic processes.

Some types of rock, in particular, quartz-containing ones, demonstrate very clear and kinetically very complex polymorphism when shock-loaded. Experimental studies of this phenomenon, including those using on-site experiments, have been ongoing for many years, but it is only in recent years that satisfactory models have been developed. Early work was limited to the effective description of flow in high-density phases, a region where the large values of the parameters $\rho_0$ and $c_0$ further reduced the region within which interpretable results could be obtained.

The table in Section 3 presents the initial values and estimated scales of $r_d$ and $r_{T\to G}$ for some typical rocks, for air, and for water. Also included for comparison are similar values for aluminum and iron, although their use as host media is unlikely to be economical.

We consider the abstract problem of an instantaneous point-like explosion in a dense medium. The solution of this problem exhibits a region in a certain neighborhood of the explosion center in which the shock wave flow can to good accuracy be treated as self-similar (with wave front pressures close to the limiting ones) and whose size is $\sim 0.1 r_d$ for typical media. We now restate the problem by considering a point-like explosion in a medium with nonlinear heat conduction as the energy transfer mechanism at large energy densities. The transition of the gasdynamic transfer mechanism then occurs at $r_{T\to G} \sim (0.06-0.09) r_d$ according to the table. In some artificial media, the ratio $r_{T\to G}/r_d$ can be somewhat less than that, but even then it is sufficiently large, thus leaving us with two distinct stages, heat-conduction and gasdynamic. We note that the timescale of the heat conduction stage is very small, and therefore, to a certain approximation, gasdynamic flows produced in strong explosions can be treated by assuming that energy is reloaded instantaneously in a region comparable in size to the radius over which the transfer mechanism changes. We are actually dealing with the problem of an instantaneous non-point-like explosion.

Therefore, developing detailed theoretical models of individual processes to describe the explosion phenomenon as a whole requires a high enough level of software power, accurate information of the thermodynamic and heat conduction properties of materials and media, and vast experimental and theoretical databases.

In the experimental studies of shock-wave flows created in the explosion, not only integral parameters but also local parameters — the ones characterizing its intensity — were used to verify physical models and mathematical codes. The shock wave itself was used to directly study the shock compressibility of various materials, including rocks from the explosion site (see Section 5).

Two other areas of computational, theoretical, and experimental explosion research were related to two classes of two-dimensional gasdynamic flows in dense media. One area was the study of how the shape of the shock wave front evolved in time following its initial distortion by inhomogeneities in central regions bordering the energy release region. It turned out, in particular, that for typical rocks, the 2 : 1, 3 : 1 prolate shape of the front in the $r_{T\to G}$ region becomes less prolate and changes phase with increasing distance, resulting in an oblate shape. However, while the front shape becomes less distorted as the wave moves away, still the distortions do not disappear, even far away at the boundaries of the gasdynamic region. The second area was concerned with shock shape distortions due to the presence of filled channels that were involved in experiments either for technological or research optimization purposes. In some cases, the shock wave had to be made to lag behind in the channel, in others, on the contrary, to take over (for example, in the gamma benchmark technique). In some experiments, accurate measurements of the wave front shape were performed and compared with the results of detailed calculations. These studies, in addition to solving specific problems, were instrumental in the development and improvement of algorithms and codes used to describe two-dimensional gasdynamic flows.

## 5. Exploring the properties of matter

The transition to underground explosions naturally led to the idea that the high-intensity processes they involve might be used to probe the properties of matter in extreme states unachievable in laboratory — the first candidate process being of course a shock wave propagating in the ambient medium. By that time, experience had already been gathered in studying shock compressibility using shock waves produced by condensed explosives [11], and extending the existing methods to high pressures difficult or impossible to achieve in laboratory experiments was a natural step to take.

The need for such data was driven by the search for wide-range equations of state that were required, in particular, for describing explosions in dense media. In the early 1960s, equations of state were developed based on either data from laboratory experiments (in the region of relatively low pressures, Ref. [11]) or data from the quantum-statistical Thomas – Fermi model (high pressures, Ref. [12]). Later, in describing the electronic component of the system, Russian researchers started using N N Kalitkin's [13] revised quantum-statistical data with regular quantum corrections. To include the ionic contribution, the one-component plasma approximation was typically used, in the form of a relation proposed by V P Kopyshev [14]. A rather big gap remained between experimental and theoretical data, where no data were available. A sufficiently strong shock wave from an underground explosion was quite capable of bridging this gap.

The most convenient way to conduct this kind of research was by employing the method of reflections, in which the shock wave passed successively through a plate of a reference substance and one of the material under study. Compounding the situation, however, was the lack of high-pressure reference data, which often restricted measurements to those of relative compressibility. For conducting underground studies, new experimental arrangements and detection schemes were designed and new types of detectors were developed. We note that because of quite favorable background conditions, many measurements used electric-contact sensors, as did many shock-wave experiments then performed in the country. The first, but nevertheless full-scale, experiment of this type was already conducted at our institute in 1966 [8]. The ability to work with big samples provided the additional possibility of accurately measuring the dynamic susceptibility of porous materials and mixture compositions [15].

Shock-wave studies using a wave in a medium are only feasible if the gasdynamic region is sufficiently large, that is, at high-yield explosions. Such experiments are expensive and relatively rare. Traditionally, they were mostly conducted at the VNII (All-Union Research Institute) of Experimental Physics, first with L V Al'tshuler and then with R F Trunin directing the shock-wave research as described above [16].

Along with just expanding the pressure range of shock-wave studies, long-base measurements proved to be a valuable option and were successfully used in a series of on-site experiments to study the kinetics of polymorphic transformations in quartz [17]. It was shown that the transition of quartz into a high-density phase in on-site experiments causes the shock wave to bifurcate, something that does not have enough time to occur in small laboratory samples. Also, the precision measurements of the shock-wave speed in a number of on-site experiments on quartz revealed that the melting of quartz affects the way in which the wave attenuates with distance. These data, together with the results of precision laboratory experiments, are used even today to better describe the behavior of quartz in dynamic processes [18]. Experiments were also made to study graphite-to-diamond transformations.

To explore shock compressibility at the extremes of high pressure, it was suggested at VNIITF to use flows in the layers bordering the $r_{T\to G}$ region. The level of pressure in such layers is always determined by the transition of the heat wave to the shock wave, and hence, by manipulating the transition temperature, waves of various intensities can be obtained. At the highest temperatures, the shock waves can reach their limit intensities $P \gtrsim 1$ Gbar, whereas by lowering temperature, waves of medium intensity $P \sim 10-100$ Mbar can be obtained at relatively large distances from the energy source. It turned out that, paradoxical as it may seem, doing research in this way is even easier at very high pressures than at high-yield explosions. However, a number of problems had to be solved first. Because this scheme places measuring units at small distances from the charge, protection from the neutron and gamma backgrounds must be provided, and because, further, contact sensors do not operate under such conditions, a special time-interval measuring technique was developed that optically determined the arrival times of the shock wave at the control levels. The technique used specially designed channels to detect light flashes that occur when the wave front arrives at the dense matter – gas interface. Because of the smaller scale of the phenomenon, smaller samples had to be used, increasing measurement accuracy and detection system requirements. Precisely this scheme provided high-precision compressibility data on a number of materials for the region close to applicability limits of quantum-statistical models.

It became clear to us in the 1970s that this pressure range needed to be studied experimentally. Although the models of matter being developed at the time were still rather simplistic, they clearly identified electron shells as a factor that could have an effect on the properties of matter close to this boundary, the size of the effect varying widely — and in some cases being very large — depending on the model used [19]. Therefore, in parallel with developing experimental techniques and preparing the master experiment, theoretical models were revised and improved [20, 21]. Data from this work were used as a reference when deciding on the goals and methodology of an on-site experiment. The 1983 master experiment produced high-precision relative compressibility data, at record pressures of hundreds of megabars, for the Fe–Al, Fe–Pb, and Pb–Fe pairs, with eight data points for each (the first metal in the pair is a reference one). Besides, additional data for these substances, as well as for water and quartz, were obtained in preparatory experiments, which confirmed that shell effects need to be studied more carefully. The choice of iron as a reference was also successful in allowing a sufficiently accurate determination of normal shock adiabats for aluminum at $P = 40-250$ Mbar and for lead at $P = 80-500$ Mbar; the adiabats were found to oscillate with respect to the quantum-statistical dependences [22, 23].

Data on mean free paths in Al and Fe, also obtained in this experiment, suggested that the results from quantum-statistical models needed to be corrected — in particular, by as much as $\sim 20-30\%$ in the temperature range $0.7-1.5$ keV at the density 1 g cm$^{-3}$ [8, 23].

Along with gasdynamic processes, neutron fluxes produced by nuclear explosions were also used in shock-wave studies. An example is the gamma benchmark method, which consists in measuring the speed of a substance (aluminum) behind the shock front at the pressure about 10 Mbar. The method involved introducing pellets with europium into the aluminum block [europium nuclei have an enhanced $(n,\gamma)$ cross section for neutrons with an energy $\varepsilon_n \lesssim 100$ eV] and it was suggested setting up the experiment such that the arrival of the shock and the neutron deceleration to the required energies be synchronized in the measuring block region. Detection was performed by using plane collimators mounted parallel to the shock-front surface moving in the sample (shock wave motion in the aluminum block was created using a magnesium-filled channel with the property that a wave propagating in the channel took over the wave in the surrounding medium). Data from this method confirmed that using iron as a reference is quite appropriate for the lower-pressure range of the relative shock compressibility measurements of aluminum [24] that were performed to assess the shell effects.

The generation of shock wave motion was yet another application of intense neutron fluxes. For this purpose, a plate of a fissionable material was introduced into experimental assemblages that were placed in such fluxes. Such measurements were made as part of experiments to study the discharge of heated matter and the associated shock wave motion. In particular, American researchers used (and we tested experimentally) a method which employed the Doppler

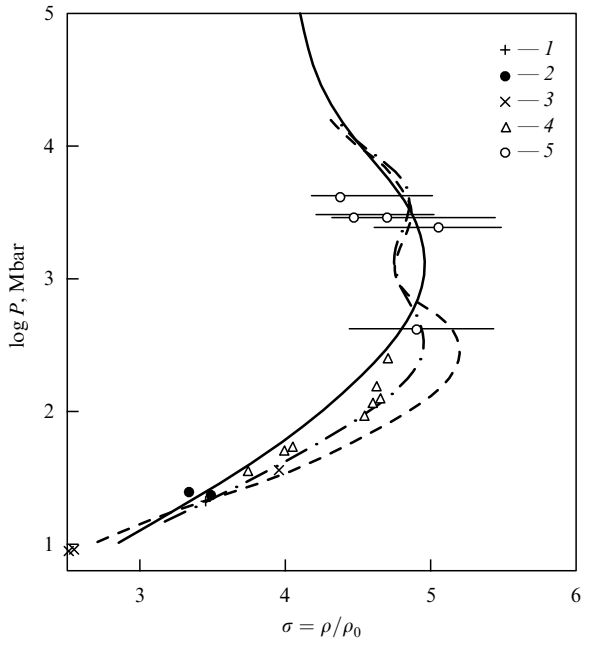


**Figure 2.** Theoretical and experimental data for the shock compressibility of Al from research using nuclear explosion experiments. Solid line is for the corrected Thomas – Fermi model [13, 14]; dot-dashed line, for the self-consistent field model [20]; and dashed line, for the Hartree – Fock – Slater model [10]. Experimental data: *1*, [16]; *2*, gamma benchmark technique [24]; *3*, [26]; *4*, precision data obtained in the region of oscillations [22]; and *5*, crude data from the quantum-statistical model in its validity range [23].

shift of neutron absorption resonances to measure the mass velocity behind the shock front [25]. Unfortunately, this method proved to be rather inaccurate.

As an example of the use of shock wave processes for the comprehensive study of matter properties, Fig. 2 shows the experimental data on the shock compressibility of Al obtained by our group and by VNIIEF [16] and American [26] researchers. For comparison, data from theoretical models are given. (We note that our results include precision data for the regions where the effect of the first electron shell is important.)

To summarize, nuclear explosion experiments provided the following data:

- the shock compressibility of a number of dense and porous materials and mixture compositions at pressures that are hard, if not impossible, to achieve in laboratory studies;
- the manifestation of electron shell effects in the shock adiabats of Al, Fe, etc.;
- phase-transition dynamics; and
- the Rosseland radiation mean free path in A and Fe.

These data are used even today as a reference in developing theoretical models of matter and constructing phenomenological equations of state.

## 6. Explosion effects on small space bodies

A clear fact that has emerged from research in different disciplines over the last decades is that ours is an epoch in which the Earth is undergoing encounters with small space bodies like asteroids and comets and their fragments — on a timescale that is longer than, comparable to, and smaller than those of a human life, a civilization, and a geological period, respectively. Such encounters may lead to catastrophic consequences — at the local, regional, or global level, depending on the size of the body — and, in the worst case scenario, may even trigger the destruction of civilization and indeed of humanity as a whole. The event rate of such encounters varies approximately inversely with the square of the size of the body.

We first discuss asteroids in some detail. So far, most of the larger — globally threatening — asteroids and only a fraction of small-size ones have been discovered. Asteroid monitoring programs are being expanded. Several asteroids with nonzero impact probabilities have been discovered. The asteroid expected to threaten Earth first is known as Apophis, discovered in 2004. In 2029, Apophis will fly by at the distance about 30,000 km from Earth, and if unfavorably deflected in its course, may collide with it in 2036. As more observations accumulate, more certain forecasts will come to replace probabilistic estimates.

Given the densely populated and dangerously technologized nature of global geography, even the events such as the Tunguska blast (with the impact energy about 15 Mt) may be extremely disastrous, so all the more Apophis, 350 m and with the predicted impact energy 1.5 Gt. Wherever it hit, there would be a catastrophe of vast proportions at the regional level — with possible devastating consequences globally. It is therefore clear that some technology should be developed to prevent this from happening. Analysis of possible collision prevention technologies has pointed to the nuclear explosive charge as the only state-of-the-art solution possible. In this case, thanks to the high energy densities involved, even a small mass can produce the necessary energy levels — allowing already existing rockets to be used to deliver these systems to the threatening objects and to deploy them on their surface in an optimal way. Clearly, the experience gathered in conducting peaceful explosions could be used to advantage in this case, as could the technology that has been developed for their description.

In the above context, three regimes in which a single nuclear explosion could be conducted for this purpose — standoff, on-surface, and buried [26] — have been explored; major energy transfer mechanisms (radiation, gasdynamic, and neutron flux) have been analyzed for their roles in this scenario; and how the deflecting momentum forms under typical conditions has been examined. It has been found that for bodies made of high-strength materials, the on-surface approach would be most efficient. However, in more complex deflection problems, other scenarios could be used as well (for example, to divert low-strength, porous bodies like the asteroid Itokawa). The efficient deflection of objects of complex shape and composition would require that multiple explosions be employed, in which case the energy of each of them, as well as their arrangement and time separations, should be optimized.

Depending on the warning time (which ranges from years for large, globally threatening bodies to days or months for those capable of inflicting regional or local damage), two orbit-modification approaches are conceivable [27].

The 'soft' approach could be used when warning times measure in years and applies to large- and medium-size bodies with sufficiently high strength properties. The energy of the explosion(s) and its (their) position(s) on the surface are chosen in such a way as to ensure the momentum transfer required for the correction and, importantly, to avoid the destruction of the body. A reliable assessment of the possible effect of the explosion requires a comprehensive study of the properties of the object, thus calling for one or more space

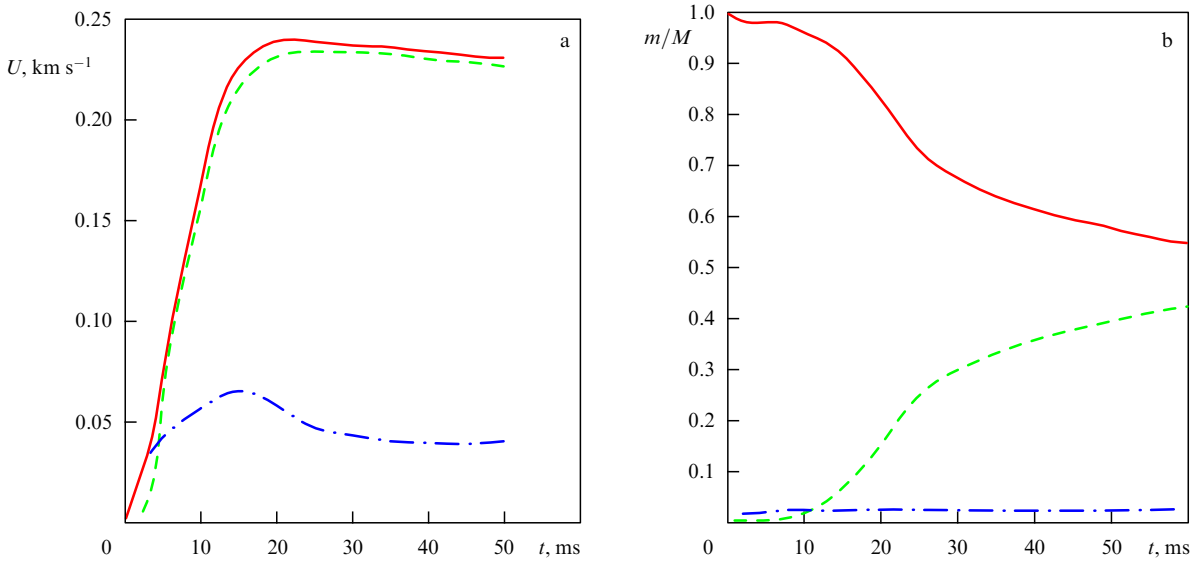


**Figure 3.** (a) Formation of the momentum of the fragment distribution: solid line, total velocity; dashed and dot-dashed lines, components perpendicular and parallel to the force, respectively; (b) Destruction of the body: solid line, intact mass fraction; dashed line, destructed fraction; dot-dashed line, mass fraction in the jet.

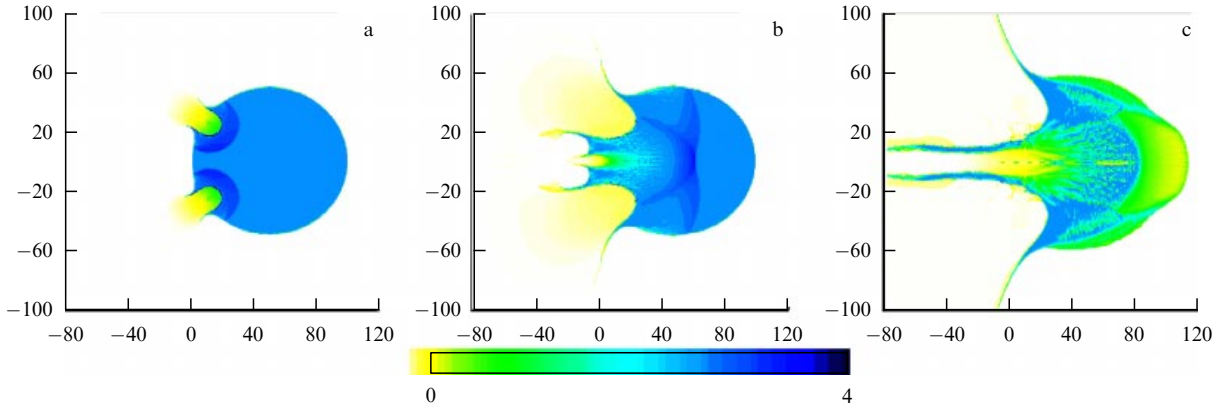


**Figure 4.** General picture of the formation of the distribution of fragments and the jet in the form of density profiles at times 3, 10, and 40 ms (for the example in Fig. 3). The axes use linear scales in meters; change in density (in g cm$^{-3}$) is represented by the linear intensity of darkening in accordance with the intensity scale shown.

research missions to be sent to it. The results thus obtained are necessary for choosing the energies, arrangement, and time pattern of the explosions. If an especially soft modification is needed, more than one series of explosions could be conducted.

The most likely and, if it arises, highly urgent scenario in the impact hazard field is one with a warning time on the scale of days or weeks. In this case, the space body would have to be impacted with a very large momentum to be prevented from hitting Earth. The body would then inevitably be dispersed, most of its mass becoming debris — which would fly by at a safe distance from the Earth — and a minor part being ejected as a jet of gas, dust, and small particles. Figure 3 depicts the formation of momentum and the destruction process for a spherical (to simplify the calculation) stony body 100 m in diameter subjected to a 100 kt buried explosion distributed over a circumference of diameter 50 m. Figure 4 depicts the destruction process by showing the density distribution for three moments in time. Although some of this material would interact with the earth's atmosphere and radiation belts and would thereby lead to some adverse effects (like anomalous magnetic phenomena and damage to satellites), this would of course be much less disastrous than what the intact body would inflict. As in the previous case, a synchronized detonation of multiple charges is also worth considering here if a more reliable prediction of what will happen is needed. The optimization criteria to be used in choosing the explosion scheme should be the reliable prevention of the impact and the minimum adverse effect on the radiation belts and the atmosphere.

By using a similar conceptual scheme, long-period comets can also be prevented from striking Earth. Unfortunately, however, the properties of comets are even less known. In particular, there is a danger of the cometary core being disintegrated by the explosion. In addition, comets move in larger orbits that are sometimes parabolic, or nearly so, the knowledge of which is typically far from certain. Furthermore, studying dangerous comets and exerting the necessary effect on them would require planning on an urgent basis of long-term, flexible, in-flight programmable missions (to

include, for example, task switching from research to interception and vice versa).

In summary, the science and technology developed for solving the problems we have outlined are in demand for the future studies of small space bodies, most importantly in the context of preventing them from colliding with Earth.

## 7. Thermonuclear burning on the surface of a neutron star

Progress in X-ray astronomy in the last three decades has opened up new possibilities for the observation of neutron stars that are in the active phase of their evolution. Among these, bodies known as X-ray bursters, identified as members of binary systems, are of special interest. The accretion of matter from its companion star ensures a sufficiently high background luminosity of the neutron star, of the order of $10^{37}$ erg s$^{-1}$, which, however, is not constant in time due to variations in the flux of the accreting matter. This enables one to estimate the matter accumulation rate $\dot{M}$ for the neutron star. A number of objects against this luminosity background show pulse flux increases by a factor in the dozens, with the leading edge around 1 s or less, the trailing edge from several to dozens of seconds, and the burst separation ranging from hours to days. The ratio of the burst energy to the overall energy of the calm stage suggests that the bursts are thermonuclear in origin. It turns out that the technology developed for describing high-intensity explosions can be very useful for describing thermonuclear neutron star bursts [28].

The matter that comes from the companion star forms a surface layer, often referred to as the atmosphere. As this matter moves deeper into the atmosphere, it changes in composition due to thermonuclear and picnonuclear reactions, and becomes stratified. In particular, some neutron stars have a layer of mainly helium formed $10^7 - 10^8$ g cm$^{-2}$ deep in their atmosphere, in which appropriate temperature conditions for the fusion of three helium atoms arise at a certain time. If conditions in this layer are relatively uniform along the entire surface, then the entire star is very soon involved in the process of thermonuclear burning (for the burning to be synchronized, even a weak adiabatic gravitational wave propagating at about $10^8$ cm s$^{-1}$ suffices). This type of regime occurs when the matter is relatively slow to accrete, and the development of this phenomenon is well modeled by one-dimensional calculations. According to our studies [29], a fundamentally important fact here is that the primary transport mechanism for the released energy is convective turbulence, which is faster than radiative heat conduction in delivering energy to the upper atmosphere and which enables helium to burn-out uniformly in the atmosphere, as shown in Fig. 5.

If the accretion rate is sufficiently high, the burning process is triggered locally (some regions of the layer being still unprepared for self-ignition). However, conditions may exist under which the burning propagates along the star surface (although the burning wave propagates much more slowly than the adiabatic gravitational wave). A feature of such bursts is distinct leading-edge oscillations. The high rotational frequency of the neutron star (up to and beyond 300 Hz) results in the burning region periodically being out of the field of view (mostly only in part) — hence the intensity modulations. After all or nearly all the surface has started burning, a similarly nonuniform cooling process follows, resulting in the falling part of the pulse being modulated.

Those still cold portions of the helium layer that border the burning region start to burn due to the flying out burning

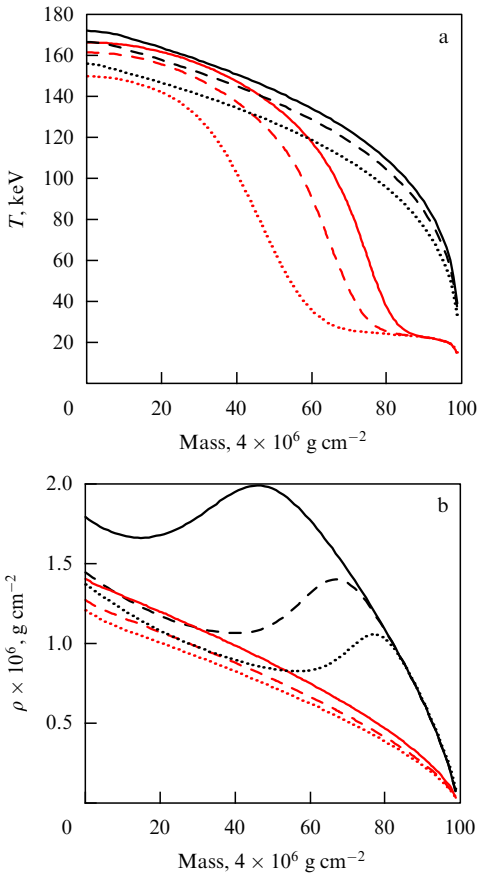


**Figure 5.** Simultaneous bursts across the surface of a neutron star atmosphere with and without taking the turbulence mixing into account (smoother curves and those with a distinct compression wave profile, respectively) for three time instants: 0.066 ms (solid lines), 0. 085 ms (dashed lines), and 0.10 ms (dotted lines). Temperature (a) and density (b) profiles as functions of mass expressed in percent of the total mass of the atmosphere (which is $4 \times 10^6$ g cm$^{-2}$).

products inflowing to the upper atmosphere. This inflow produces some additional compression and increases the temperature at the bottom of the helium layer bordering the burning region. This provides conditions for ignition, and this configuration moves over the surface of the neutron star. In this way, a self-maintaining thermonuclear burning regime forms due to the gravitational compression of matter by burning products flowing from above. This mechanism of burning in the helium layer was investigated using the two-dimensional codes TIGR (finite-difference Euler – Lagrange method) and MPM (modified particle method) [29]. Figure 6 shows modeling results for this process. The estimated burning wave speed, $5 \times 10^6 - 10^7$ cm s$^{-1}$, is in good agreement with the observational data.

One further point to mention is that a localized thermonuclear burst excites an adiabatic gravitational wave propagating along the atmosphere. The focusing of this wave in the antipodal area involves an additional inflow of matter [30], with the possible result that under favorable conditions, thermonuclear ignition synchronized with the primary one is triggered in the antipode, with thermonuclear burning therefore propagating over the star surface from two regions. This type of regime presumably occurs for bursters with the modulation frequency about 600 Hz.

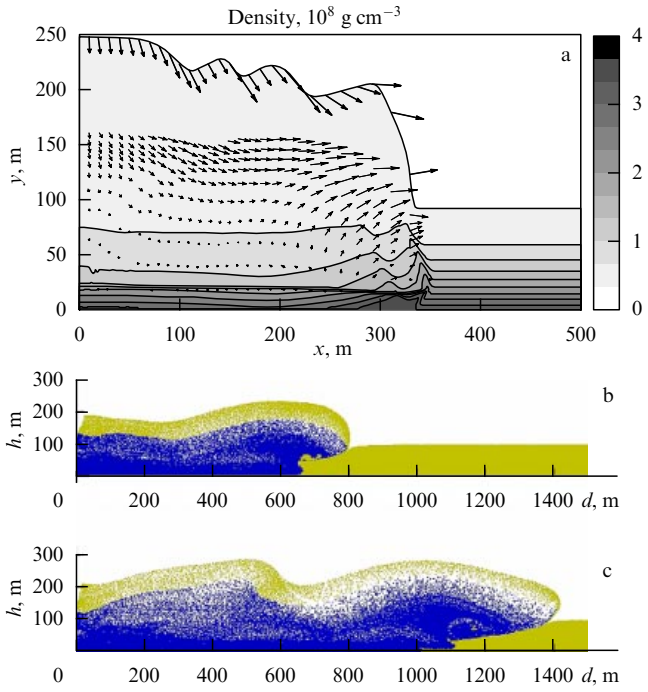


**Figure 6.** Formation of a thermonuclear burning wave in the gravitational self-shrinking regime. Panel (a) (obtained using the TIGR code for the atmospheric thickness $1.8 \times 10^7$ g cm$^{-2}$) shows density profiles in units of $10^8$ g cm$^{-3}$ (linear intensity scale of densities is shown on the right) and the velocity vector field (arrows) reflecting the inflow of matter and increase in the density of the lower layer. Panel (b) is obtained using the MPM code for the atmospheric thickness $1.8 \times 10^8$ g cm$^{-2}$. Light points correspond to the initial substance, helium; burning products are shown dark. The inflow of burning products along the upper boundary of the atmosphere is readily seen. $h$ is the height of the atmosphere and $d$ is the traveled path.

This then is another example of where the technology developed for describing explosion phenomena can be usefully applied.

## 8. Conclusion

The study and use of high-intensity processes involved in nuclear explosions has provided valuable insights both into how these processes evolve and into the relevant properties of the media involved.

For the first time in terrestrial experiments, high-temperature thermal processes due to nonlinear radiative heat conduction were explored and used. Under the conditions of energy transfer changing from the heat to gasdynamic regime, heat conduction data for materials in high-temperature dense plasma environment were obtained. These data stimulated further work on theoretical models, which, in this context, are the primary source of information on the heat conduction properties of materials in this field.

The shock wave flow that results from a regime changeover is the most intense adiabatic flow experimentally achievable for such high-density media. It was shown that strong explosions in media of currently accessible densities, in fact, show no region of self-similar motion — first, because the region where energy is transferred by heat is relatively large (making the effective energy release 'non-point-like'); and, second, because the region of gasdynamic motion is relatively small. The subsequent evolution of the shock is strongly affected by such factors as the quantum mechanical nature of particle interactions in dense matter, phase transition phenomena (melting and, possibly, polymorphic transitions), and strength properties. The evolution of polymorphic transition is often complicated by kinetic effects.

Shock waves from nuclear explosions were directly used to extend shock compressibility measurements of dense materials to the high-pressure range, as well as for compressing highly porous and mixture samples. Through the use of such explosions, unique data on the shock compressibility of a number of materials and rocks at pressures beyond the laboratory scale were obtained. Moreover, precision shock compressibility measurements at the applicability limit of quantum-statistical models were made, which not only confirmed that electron shell effects influence the course of a normal shock adiabat but also provided an accurate description of the shock adiabat behavior in the region of the first oscillation for Al and Fe. Detailed studies of shock wave attenuation in massive quartz revealed the influence of melting processes and enabled the observation of the two-wave mode in the region of dynamic transformation of $\alpha$-quartz to the high-density phase — a regime that has not been observed in laboratory experiments. These data are being used even now in constructing more accurate theoretical models of the behavior of dense matter both at high pressures and temperatures and in the region where phase transitions show up and strength properties become relevant.

Importantly, there was a strong preparatory component to research on nuclear explosions, including a complex of laboratory experiments (on low-pressure shock compressibilities and on modeling some relevant processes) and work on the mathematical simulation of both individual processes and the explosion as a whole based on the already existing physical models, software packages, and adequate computational means. In turn, the results of on-site experiments were used to improve and develop these tools.

Thus, on the one hand, the experimental results stimulated the development and improvement of physical and mathematical models and of computer programs, whereas on the other hand, the results of mathematical simulation allowed more sophisticated experiments, extended the scope and range of research, and provided more accurate experimental data. In fact, research into processes involved in nuclear explosions resulted in a scientific technology for probing the physics of high energy densities — a technology in which physical models and simulation method development and on-site and laboratory experimentation are naturally integrated. As a result, a vast research potential was built up, so vast, indeed, that even today this technology is being successfully developed, taking advantage of the power of modern experimental techniques, using advanced simulation software and enhanced computational capabilities, and finding ever more applications. To illustrate these points, two examples are given in the text.

The first example is concerned with the study of nuclear explosion effects on Earth-threatening space objects like asteroids and comets and their fragments. The effects of standoff, on-surface, and buried explosions have been examined, and the most effective ways in which the energy and momentum of an explosion can be transferred to a threatening body to prevent its collision with Earth (specifically, two extreme scenarios — a 'soft' orbit modification and a high-speed dispersion of the body) have been considered. At the current level of technology, nuclear explosions are the only (and also quite feasible) way to prevent dangerous collisions.

The other example is pulsed thermonuclear burning on the surface of a neutron star in a low-mass binary system. For this scenario, the convective-turbulence-mediated transfer of the released energy is shown to be fundamentally important. If the accretion rate is sufficiently low, this mechanism accelerates the delivery of energy to the surface and leads to the uniform burnout of the thermonuclear fuel. For a high accretion rate, the burnout process starts in the region that is most prepared for this and propagates along the surface in the form of a wave in the gravitational self-compression regime.

The list of examples could be extended to include both low-energy (but high-power) explosive processes (found, for example, in superintense laser pulses) and still higher energy ranges (e.g., supernova and hypernova explosions).

## References


1. Sedov L I *Dokl. Akad. Nauk SSSR* **52** 17 (1946); *Prikl. Mat. Mekh.* **10** 241 (1946); *Metody Podobiya i Razmernosti v Mekhanike* (Similarity Methods and Dimensionalities in Mechanics) (Moscow: Nauka, 1987) [Translated into English (Moscow: Mir Publ., 1982)]
2. Stanyukovich K P *Neustanovivshiesya Dvizheniya Sploshnoi Sredy* (Unsteady Motion of Continuous Media) (Moscow: GITTL, 1955) [Translated into English (New York: Pergamon Press, 1960)]
3. Taylor G *Proc. R. Soc. London Ser. A* **201** 175 (1950)
4. Basov N G, Lebo I G, Rozanov V B *Fizika Lazernogo Termoyadernogo Sinteza* (Physics of Laser Fusion) (Moscow: Znanie, 1988)
5. Zel'dovich Ya B, Kompaneets A S "K teorii rasprostraneniya tepla pri teploprovodnosti, zavisyashchei ot temperatury" ("On the theory of heat transfer with a temperature-dependent heat conductivity"), in *Sbornik, Posvyashchennyi 70-letiyu Akademika A.F. Ioffe* (Collection in Honor of the 70th Birthday of Academician A.F. Ioffe) (Moscow: Izd. AN SSSR, 1950)
6. Zel'dovich Yu B, Raizer Yu P *Fizika Udarnykh Voln i Vysokotemperaturnykh Gidrodinamicheskikh Yavlenii* (Physics of Shock Waves and High-Temperature Hydrodynamic Phenomena) (Moscow: Nauka, 1966) p. 519 [Translated into English: *Elements of Gasdynamics and the Classical Theory of Shock Waves* (New York: Academic Press, 1968)]
7. Kompaneets A S, Lantsburg E Ya *Zh. Eksp. Teor. Fiz.* **43** 234 (1962) [*Sov. Phys. JETP* **16** 167 (1963)]
8. Avrorin E N, Simonenko V A, Shibarshov L I *Usp. Fiz. Nauk* **176** 449 (2006) [*Phys. Usp.* **49** 432 (2006)]
9. Mikhailov V N et al. (Eds) *Yadernye Ispytaniya SSSR* (Nuclear Weapons Tests of the USSR) Vol. 1, 2 (Sarov: Izd. PFYaTs — VNIIEF, 1997)
10. Nikiforov A F, Novikov V G, Uvarov V B *Kvantovo-statisticheskie Modeli Vysokotemperaturnoi Plazmy: Metody Rascheta Rosselandovykh Probegov i Uravnenii Sostoyaniya* (Quantum Statistical Models of High Temperature Plasma and Methods for Calculating Rosseland Mean Free Paths and Equations of State) (Moscow: Fizmatlit, 2000) [Translated into English: *Quantum-statistical Models of Hot Dense Matter: Methods for Computation Opacity and Equation of State* (Basel: Birkhäuser Verlag, 2005)]
11. Al'tshuler L V *Usp. Fiz. Nauk* **85** 197 (1965) [*Sov. Phys. Usp.* **8** 52 (1965)]; Al'tshuler L V et al. *Usp. Fiz. Nauk* **166** 575 (1996) [*Phys. Usp.* **39** 539 (1996)]
12. Latter R *Phys. Rev.* **99** 1854 (1955)
13. Kalitkin N N, Kuz'mina L V "Tablitsy termodinamicheskikh funktsii veshchestv pri vysokikh kontsentratsiyakh energii" ("Tables of thermodynamic functions of materials at high energy concentrations), Preprint No. 35 (Moscow: IPM AN SSSR, 1975)
14. Kopyshev V P "O termodinamike yader odnokomponentnogo veshchestva" ("On the thermodynamics of nuclei in a one-component material"), in *Chislennye Metody Mekhaniki Sploshnoi Sredy* (Numerical Methods in Mechanics of Continua) Vol. 8, Issue 6 (Novosibirsk: VTs ITPM SO AN SSSR, 1977) p. 54
15. Vildanov V G et al., in *Shock Compression of Condensed Matter — 1995* Vol. 1 (AIP Conf. Proc., No. 370, Eds S C Schmidt, W C Tao) (Woodbury, NY: American Institute of Physics, 1996) p. 121
16. Trunin R F *Usp. Fiz. Nauk* **164** 1215 (1994) [*Phys. Usp.* **37** 1123 (1994)]
17. Zhugin Yu N et al. *Fiz. Zemli* (6) 46 (1999) [*Izv., Phys. Solid Earth* **35** 478 (1999)]
18. Petrovtsev A V et al. "Equation of state and phase diagram quartz", in *Shock Compression of Condensed Matter — 2005* (AIP Conf. Proc., CP 845, Ed. M D Furnish) (Melville, NY: American Institute of Physics, 2006) (in press)
19. Simonenko V A "Vozmozhnosti izucheniya uravnenii sostoyaniya plotnykh veshchestv v oblasti proyavleniya obolochechnykh effektov" ("Prospects for equation of states studies on dense materials in the strong shell effect region") *Voprosy At. Nauki Tekh. Ser. Teor. Prikl. Fiz.* ((1)) 3 (1984)
20. Sin'ko G V "Raschety termodinamicheskikh funktsii prostykh veshchestv na osnove uravneniya sostoyaniya samosoglasovannogo polya" ("Calculation of thermodynamic functions for simple substances using a self-consistent field equation of state"), in *Chislennye Metody Mekhaniki Sploshnoi Sredy* (Numerical Methods in Mechanics of Continua) Vol. 10, Issue 3 (Novosibirsk: VTs ITPM SO AN SSSR, 1979) p. 124
21. Andriyash A V, Simonenko V A "Otsenka vliyaniya obolochechnykh effektov na termodinamicheskie svoistva prostykh veshchestv" ("Estimating shell effects on the thermodynamic properties of simple substances") *Voprosy At. Nauki Tekh. Ser. Teor. Prikl. Fiz.* (2(2)) 52 (1984)
22. Avrorin E N et al. *Zh. Eksp. Teor. Fiz.* **93** 613 (1987) [*Sov. Phys. JETP* **66** 347 (1980)]
23. Vodolaga B K, Simonenko V A "Udarnye issledovaniya i matematicheskoe modelirovanie" ("Shock studies and mathematical modeling"), in *Fiziko-Khimicheskie Svoistva Veshchestva* (Physical and Kinematic Properties of Matter) (Editors-in-Chief A A Samarskii, N N Kalitkin) (Moscow: Nauka, 1989)
24. Simonenko V A et al. *Zh. Eksp. Teor. Fiz.* **88** 1452 (1985) [*Sov. Phys. JETP* **61** 869 (1985)]
25. Ragan C E (III), Silbert M G, Diven B C *J. Appl. Phys.* **48** 2860 (1977)
26. Simonenko V A et al. "Defending the Earth against impacts from large comets and asteroids", in *Hazards Due to Comets and Asteroids* (Ed. T Gehrels) (Tucson: Univ. of Arizona Press, 1994) p. 929
27. Simonenko V A "O korrektirovke dvizheniya asteroidov s pomoshch'yu yadernykh vzryvov" ("Using nuclear explosions to divert asteroids") *Rossiiskii Kosmos* (3) (2002); Simonenko V A, Gadzhieva V V, Elsukov V P "Ob opasnosti stolknoveniya kosmicheskikh tel s Zemlei i ee predotvrashchenii" ("The danger and prevention of Earth's encounters with space bodies"), in *Zababakhinskie Nauchnye Chteniya: Mezhdunar. Konf., 8 – 12 Sent. 2003, Snezhinsk, Chelyab. obl., Russia. Tezisy* (Zababakhin Scientific Talks: Intern. Conf. 8 – 12 Sep. 2003, Snezhinsk, Chelyabinsk region, Russia. Theses) (Snezhinsk: Izd. RFYaTs — VNIITF, 2003) p. 214
28. Simonenko V A "Neitronnye zvezdy i yadernye vzryvy" ("Neutron stars and nuclear explosions"), in *Voprosy Sovremennoi Tekhnicheskoi Fiziki: K 70-letiyu so Dnya Rozhdeniya Akad. E.N. Avrorina. Izbrannye Trudy RFYaTs — VNIITF* (Problems in Modern Engineering Physics: on the Occasion of the 70th Birthday of Academician E.N. Avrorin. Selected Works of RFYaTs — VNIITF) (Ed. G N Rykovanov, Compiled by G N Rykovanov et al.) (Snezhinsk: Izd. RFYaTs — VNIITF, 2002) p. 391
29. Simonenko V A et al. "Termoyadernye vspyshki neitronnykh zvezd: usloviya vozniknoveniya i rezhimy goreniya" ("Thermonuclear bursts of neutron stars: conditions for and regimes of combustion"), in *Zababakhinskie Nauchnye Chteniya: Mezhdunar. Konf. 8 – 12 Sent. 2003, Snezhinsk, Chelyab. obl., Russia. Tezisy* (Zababakhin Scientific Talks: Intern. Conf. 8 – 12 Sep. 2003, Snezhinsk, Chelyabinsk region, Russia. Theses) (Snezhinsk: Izd. RFYaTs — VNIITF, 2003) p. 5
30. Simonenko V A, Shishkin N I "Termoyadernye vspyshki neitronnykh zvezd: initsiirovanie vtorichnoi volny goreniya v antipode oblasti pervichnogo initsiirovaniya" ("Thermonuclear bursts of neutron stars: of the secondary burning wave in the antipode area

of primary ignition''), in *Zababakhinskie Nauchnye Chteniya: Mezhdunar. Konf. 8–12 Sent. 2003, Snezhinsk, Chelyab. obl., Russia. Tezisy* (Zababakhin Scientific Talks: Intern. Conf. 8–12 Sep. 2003, Snezhinsk, Chelyabinsk region, Russia. Theses) (Snezhinsk: Izd. RFYaTs — VNIITF, 2003) p. 106

PACS numbers: 75.30.Sg, **75.80.+q**, 81.30.Kf
DOI: 10.1070/PU2006v049n08ABEH006081

# Magnetic shape-memory alloys: phase transitions and functional properties

V D Buchelnikov, A N Vasiliev, V V Koledov, S V Taskaev, V V Khovaylo, V G Shavrov

## 1. Introduction

The discovery of the effect of giant deformations due to a magnetically induced rearrangement of martensite twins in Heusler alloys $Ni_2MnGa$ [1] attracted significant attention to shape-memory alloys. As a result of intense research in this field, magnetically induced strains as large as 10%, which can be controlled by a magnetic field of about 1 T, have been realized in Ni-Mn-Ga single crystals, and a number of new families of ferromagnets with a shape-memory effect have been revealed [2].

In this report, we review the art and science of theoretical and experimental investigations of phase transitions in ferromagnetic Heusler alloys with the shape-memory effect and of related giant changes in entropy and strain under the effect of an applied magnetic field. Attention is mainly paid to new results concerning the investigations of Ni-Mn-Ga alloys. In particular, we analyze the results of investigations of the specific features of the phase diagram of these alloys and their physical properties in the nanocrystalline state.

## 2. Magnetic and structural phase transitions

### 2.1 Phenomenological theories

To describe phase transitions in Ni-Mn-Ga alloys, we first consider the Landau functional [3–8]

$$
\begin{aligned}
F = {} & -Ae_1 + \frac{1}{2}\,A_0 e_1^2 + \frac{1}{2}\,a_1(e_2^2+e_3^2) + De_1(e_2^2+e_3^2) \\
& + \frac{1}{3}\,be_3(e_3^2-3e_2^2) + \frac{1}{4}\,c(e_2^2+e_3^2)^2 + \frac{1}{2}\,A_1|\psi|^2 + \frac{1}{4}\,A_2|\psi|^4 \\
& + \frac{1}{6}\,C_0|\psi|^6 + \frac{1}{6}\,C_1\left[\psi^6 + (\psi^*)^6\right] \\
& + \left(\frac{1}{\sqrt{3}}\,D_1e_1 + \frac{2}{\sqrt{6}}\,D_2e_3 + D_3e_4\right)|\psi|^2 + \frac{1}{2}\,\alpha_1\mathbf{m}^2 + \frac{1}{4}\,\delta_1\mathbf{m}^4 \\
& + K(m_x^2m_y^2 + m_y^2m_z^2 + m_z^2m_x^2) + \frac{1}{\sqrt{3}}\,B_1e_1\mathbf{m}^2 \\
& + B_2\left[\frac{1}{\sqrt{2}}\,e_2(m_x^2-m_y^2) + \frac{1}{\sqrt{6}}\,e_3(3m_z^2-\mathbf{m}^2)\right] \\
& + B_3(e_4m_xm_y + e_5m_ym_z + e_6m_zm_x) \\
& + \left[N_1\mathbf{m}^2 + N_2\left(m_z^2 - \frac{1}{3}\,\mathbf{m}^2\right) + N_3m_xm_y\right]|\psi|^2 + Pe_1\,, \quad (1)
\end{aligned}
$$

where $e_i$ are the linear combinations of the strain tensor components: $e_1 = (e_{xx}+e_{yy}+e_{zz})/\sqrt{3}$, $e_2 = (e_{xx}-e_{yy})/\sqrt{2}$, $e_3 = (2e_{zz}-e_{yy}-e_{xx})/\sqrt{6}$, $e_4 = e_{xy}$, $e_5 = e_{yz}$, $e_6 = e_{zx}$; $\psi$ is the order parameter that describes the modulation of the crystal lattice and is related to the displacement vector $\mathbf{u}$ along the $[\bar{1}10]$ axis as $\mathbf{u}(\mathbf{r}) = |\psi|\mathbf{p}\sin(\mathbf{kr}+\varphi)$, where $\psi = |\psi|\exp(\mathrm{i}\varphi)$, $\mathbf{k} = (1/3)[110]$, and $\mathbf{p}$ is the polarization vector; $A$ is a coefficient proportional to the thermal expansion coefficient; $A_0 = (c_{11}+2c_{12})/\sqrt{3}$ is the bulk elasticity modulus; $a_1$, $b$, $D$, and $c_1$ are linear combinations of elasticity moduli of the second, third, and fourth orders,

$$
a_1 = c_{11} - c_{12}\,, \qquad b = \frac{c_{111} - 3c_{112} + 2c_{123}}{6\sqrt{6}}\,,
$$

$$
D = \frac{c_{111} - c_{123}}{2\sqrt{3}}\,, \qquad c = \frac{c_{1111} + 6c_{1112} - 3c_{1122} - 8c_{1123}}{48}\,;
$$

$\mathbf{m} = \mathbf{M}/M_0$ is the unit magnetization vector; $M_0$ is the saturation magnetization; $B_1$ is the constant of volume (exchange) magnetostriction; $B_2$ and $B_3$ are the constants of anisotropic (relativistic) magnetostriction; $K$ is the first constant of cubic anisotropy; $\alpha_1$ and $\delta_1$ are the exchange constants; $A_1$, $A_2$, $C_0$, and $C_1$ are the coefficients of the expansion of the functional into a series in powers of the modulation order parameter $\psi$; $D_i$ are the coupling coefficients of the deformation and modulation order parameters; $N_i$ are the coupling constants of the modulation order parameter to the magnetization; and $P$ is the hydrostatic pressure.

The equilibrium states of a cubic ferromagnet can be determined from thermodynamic potential (1) using the standard minimization procedure. The solution of this problem, which can be found both analytically and numerically, has been obtained in several works (see [2] and the references therein).

We note that in $Ni_{2+x}Mn_{1-x}Ga$ alloys, the sign of the first cubic anisotropy constant $K$ depends on the composition [9, 10]. Therefore, the cases where $K > 0$ and $K < 0$ must be considered within a theoretical description of phase transitions (see Refs [66, 67, 91, 200–210] and [211–215] in [2] for $K < 0$ and $K > 0$, respectively).

Investigations of the effect of magnetostriction and modulation of the crystal lattice on the phase transition in Ni-Mn-Ga alloys show that, with the modulation order parameter taken into account, the martensitic transformation is accompanied by either premartensitic or intermartensitic phase transitions [7, 11].

Taking the magnetoelastic interaction into account leads to the appearance of a domain of the existence of combined magnetic and structural (magnetostructural) phase transitions in the phase diagram of $Ni_{2+x}Mn_{1-x}Ga$ alloys [12, 13]. Estimates show that the magnetostructural phase transition in the temperature–composition ($T-x$) phase diagram is realized in a very narrow range of $x$. Recent experimental studies of the $T-x$ phase diagram of Ni-Mn-Ga alloys in a wider composition range [14] showed that the magnetostructural transition is realized in a rather wide composition interval from $x = 0.18$ to $x = 0.27$ (Fig. 1). In this concentration range, the alloys undergo a transition from a cubic paramagnetic phase into a tetragonal ferromagnetic phase. In this transformation, we can therefore neglect the magnetostriction related to anisotropy and consider only the volume magnetostriction, which is usually large just in the region of a magnetic phase transition. The phase diagram

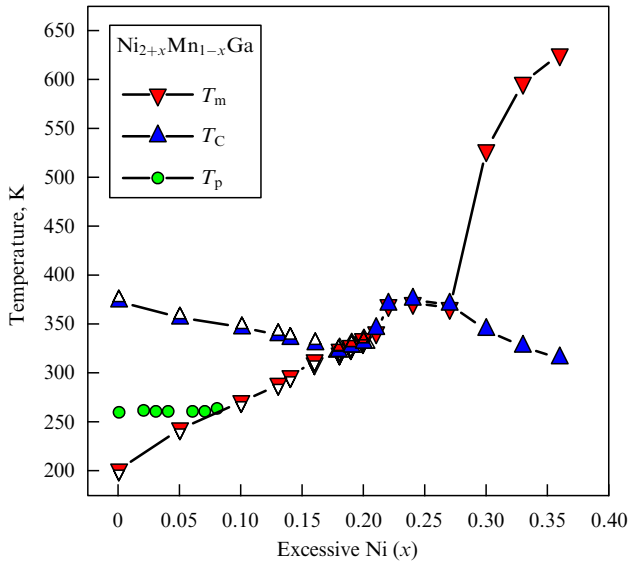


**Figure 1.** Temperatures of martensitic ($T_m$), magnetic ($T_C$), and premartensitic ($T_p$) phase transitions as functions of excessive Ni in $Ni_{2+x}Mn_{1-x}Ga$ alloys [14–16].

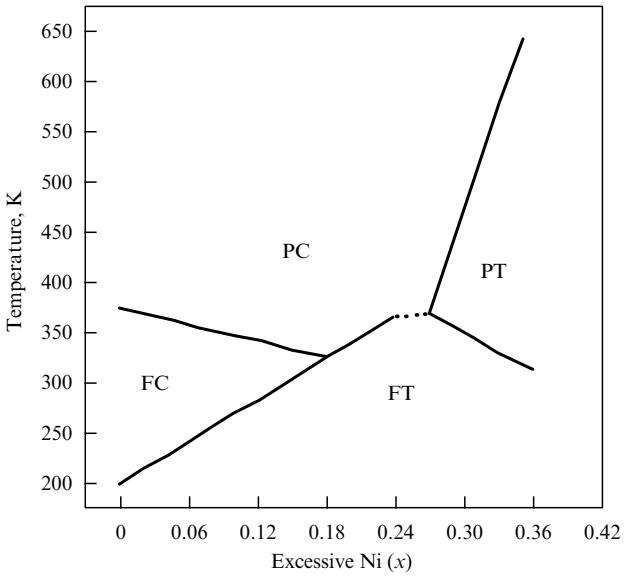


**Figure 2.** Theoretical phase diagram of $Ni_{2+x}Mn_{1-x}Ga$ alloys in the concentration range $0 < x < 0.36$ with the volume magnetostriction taken into account. Solid straight lines correspond to phase transition lines [8]; PC and PT stand for paramagnetic cubic and tetragonal phases, respectively; FC and FT mean ferromagnetic cubic and tetragonal phases, respectively.

of $Ni_{2+x}Mn_{1-x}Ga$ alloys with volume magnetostriction taken into account was constructed in [8]. To estimate the possibility of the existence of a magnetostructural transition interval, we must know the magnitude of the volume magnetostriction $B_1$. It was determined in [14, 17] from a comparison of the theoretical jump in the thermal expansion coefficient ($\Delta\varkappa = \varkappa_F - \varkappa_P = B_1\alpha_0/(\sqrt{3}A_0T_C^0\delta)$ [14]) and its experimentally determined value for the stoichiometric $Ni_2MnGa$ alloy. Here, $\varkappa_F$ and $\varkappa_P$ are the respective thermal expansion coefficients in the ferromagnetic and paramagnetic phases; $\alpha_0$ is the coefficient in the series expansion (in the temperature) of the renormalized (with respect to magnetostriction) exchange constant $\alpha_1$ near the Curie temperature dependent on the composition $x$: $T_C(x) = T_C^0 - \gamma x$, where $\gamma$ is a coefficient determined from experiment; $\alpha_1 = \alpha_0(T - T_C)/T_C^0$, $T_C^0$ is the Curie temperature for the stoichiometric composition; and $\delta$ is the $\delta_1$ constant renormalized with respect to magnetostriction. The magnetostriction magnitude thus determined turned out to be $B_1 = 21 \times 10^9$ erg cm$^{-3}$. This value of the magnetostriction constant permitted us to theoretically estimate the composition interval of the existence of the magnetostructural phase transition as $\Delta x = x_{fin} - x_{in} \approx 0.08$, which agrees well with experimental data (see Fig. 1).

The theoretical $T-x$ phase diagram with only volume magnetostriction take into account and a linear dependence of the martensitic and magnetic phase transition temperatures on the composition assumed is shown in Fig. 2 by solid lines. It is seen that there is good agreement between theory and experiment. It follows from experimental data that on the line of the magnetostructural phase transition near $x \approx 0.27$, a substantial deviation from the linear dependence is observed; the corresponding segment is shown in Fig. 2 by a dashed line.

### 2.2 Magnetostructural transition

An analysis of the effect of volume magnetostriction on the phase diagram of $Ni_{2+x}Mn_{1-x}Ga$ alloys performed in [8, 14, 17] shows that it can well explain the existence of a sufficiently large range of compositions where a coupled magnetostructural transition can occur in these alloys.

From the experimental standpoint, this feature of the phase diagram of $Ni_{2+x}Mn_{1-x}Ga$ alloys can be explained as follows. The available experimental data show that the compositional dependence of the martensitic transformation temperature $T_m$ in Ni-Mn-Ga alloys correlates with the concentration of valence electrons $e/a$; therefore, these alloys can be classified as Hume–Rothery alloys [18]. The martensitic transition occurs as a result of contact of the Fermi surface with the Brillouin zone boundary [19]. Such a model suggests that a change in the number of valence electrons and the modification of the Brillouin zone boundary are the principal factors responsible for the appearance of structural instabilities in these alloys. Neglecting the effects of hybridization and other factors, such as the difference in the electronegativities [20], we can expect a linear variation of $T_m$ with composition caused by changes in the number of valence electrons and chemical pressure, which is indeed observed in some composition intervals in $Ni_{2+x}Mn_{1-x}Ga$ [15], $Ni_{2+x}MnGa_{1-x}$ [21], and $Ni_2Mn_{1+x}Ga_{1-x}$ [22] alloys. However, this scenario is fulfilled when approaching the Curie point, because the volume magnetostriction substantially affects the lattice parameters. In this sense, the peak of the thermal expansion coefficient observed at the Curie point $T_C$ can be regarded as a potential barrier to a further increase in the martensitic transformation temperature $T_m$, which becomes 'blocked' at the temperature of this peak. A further change in $T_m$ correlates with a change in the Curie temperature $T_C$; i.e., $T_m$ and $T_C$ are interdependent in some composition interval. To separate these phase transitions, we must reach a concentration $e/a$ that is sufficient to overcome this barrier caused by the volume magnetostriction.

The coincidence of the temperatures of the martensitic and magnetic transitions $T_m$ and $T_C$ is also observed in other ferromagnetic shape-memory alloys, e.g., Co-Ni-$X$ ($X$ = Al,

Ga) [23, 24], Ni-Fe-Ga [25, 26], and Ni-Mn-$X$ ($X$ = In, Sn, Sb) [27, 28]. In Ni-Mn-Ga, the merging of $T_m$ and $T_C$ is observed for various sections of the ternary phase diagram. In the $Ni_{2+x}Mn_{1-x}Ga$ system, $T_m$ and $T_C$ coincide in the alloy of composition $Ni_{2.18}Mn_{0.82}Ga$ [15]. This effect also occurs in $Ni_2Mn_{1+x}Ga_{1-x}$ alloys with extra Mn instead of Ga [22] and in alloys where Ni atoms are partially replaced by Ga atoms [21].

### 2.3 Phase diagrams of ferromagnetic Heusler alloys with a shape-memory effect

The results of studies of $Ni_{2+x}Mn_{1-x}Ga$ and $Ni_2Mn_{1+x}Ga_{1-x}$ alloys showed their universal tendency to increase $T_m$ and decrease $T_C$ with a deviation of the alloy composition from stoichiometric. The increase in $T_m$ in these alloys can be related to an increase in the electron concentration $e/a$. Although the first-principle calculations [29] of nonstoichiometric $Ni_2MnGa$ alloys show that the change in the electronic structure caused by deviations of the alloy composition from stoichiometric cannot be described in terms of the 'rigid-band' model, the empirical dependence between the electron concentration and the martensitic transition temperature [18] indicates the applicability of this model. The decrease in $T_C$ that is observed in $Ni_{2+x}Mn_{1-x}Ga$ and $Ni_2Mn_{1+x}Ga_{1-x}$ with increasing $x$ is likely to be due to different factors. In the Ni-Mn-Ga alloys, the magnetic moment, which is equal to $\sim 4\,\mu_B$, is caused by Mn atoms, and hence the $T_C$ decrease in $Ni_{2+x}Mn_{1-x}Ga$ can be explained by the dilution of the magnetic subsystem due to a decrease in the Mn content. For alloys with an excess of Mn atoms (in $Ni_2Mn_{1+x}Ga_{1-x}$), the weakening of exchange interactions can be due to an antiferromagnetic interaction of the excessive Mn atoms [30], although this assumption needs an experimental test. A systematic study of magnetic properties of $Ni_{2+x}Mn_{1-x}Ga$ alloys [31] showed that both the interatomic spacing and the overlap of electron orbitals play an important role in the changes of the exchange parameters upon the structural transformation and that the exchange interactions are stronger in the martensitic state.

The phase diagrams of other ferromagnets with a shape-memory effect have been studied in less detail. The available experimental results indicate a common tendency in the behavior of the structural phase transition upon deviations from the stoichiometric composition: in all ferromagnetic shape-memory Heusler alloys, the temperature of the martensitic transformation increases with increasing the electron concentration $e/a$ [23, 25, 27]. This feature indicates that, evidently, the structural instability in Heusler alloys has a universal origin.

As is known, premartensitic and intermartensitic transitions are observed in Ni-Mn-Ga alloys in addition to the martensitic transformation [2]. The premartensitic transition, which manifests itself in the modulation of the crystal structure of the austenitic phase with the lattice symmetry preserved, is observed for Ni-Mn-Ga compositions close to stoichiometric. The results of some works suggest that either the premartensitic transition or clearly pronounced pretransition phenomena also exist in some compositions of the Ni-Fe-Ga system [32–34]. In other ferromagnets with the shape-memory effect, no premartensitic phase transitions are observed, to the best of our knowledge. Apart from the Ni-Mn-Ga system, the existence of intermartensitic transitions from one crystallographic modification of the martensitic phase into another was also reported for Ni-Fe-Ga [35, 36] and Ni-Mn-$X$ ($X$ = In, Sn) [27] alloys. Because both the premartensitic and, as a rule, martensitic phases are modulated, the formation of superstructural motifs is ascribed to nesting features of the Fermi surface [37, 38].

### 2.4 Phase transitions in the nanocrystalline state

Physical properties of solids change fundamentally when a nanocrystalline structure is created in them by severe plastic deformation, i.e., by refining crystallites to dimensions of 10–100 nm under high pressure [39]. The authors of Refs [40–42] obtained nanocrystalline ferromagnetic shape-memory alloys of the Ni-Mn-Fe-Ga system and studied the effect of the nanostructure on the martensitic transformation and magnetic ordering and then the effect of subsequent annealings on them. It was shown by electron microscopy that the sample subjected to severe plastic deformation consists of very small-dimension ($< 5$ nm) crystallites that have no distinct boundaries between them. The subsequent annealing restores the crystallite structure.

Figure 3a displays the temperature dependence of the magnetization of the initial coarse-grained sample. The anomalies at $T_C = 350$ K, $T_m = 290$ K, and $T_I = 230$ K correspond respectively to the Curie temperature and martensitic and intermartensitic transitions. In the nanocrystalline state, the alloy under consideration does not exhibit ferromagnetic properties. The subsequent annealing leads first to restoration of the ferromagnetic ordering and then to restoration of the anomalies related to the structural transition ($T_m$). However, the intermartensitic transition is not restored (Fig. 3b), which is also confirmed by measurements of electric conductivity.

The disappearance of a long-range order and the suppression of structural phase transitions can arguably be explained by atomic disordering of the alloy in the process of severe plastic deformation and by the effect of the crystallite size on the formation of a magnetically ordered state. A similar situation was revealed in a series of papers [43–45] devoted to the investigation of the effect of the degree of ordering on magnetism and structural transformation of $Ni_2MnGa$ films obtained in a quasiamorphous state by vacuum deposition onto a cooled substrate.

## 3. Functional properties

### 3.1 Magnetomechanical effects

If the magnetization of the martensitic phase differs from the magnetization of the austenitic phase, the application of a magnetic field leads to a shift in the temperature of the structural transformation, i.e., to a stabilization of the phase with a larger magnetization [46]. This effect can be used to obtain giant magnetostrains in the temperature range of the martensitic transformation. Investigations in Refs [47–49] were aimed at creating functional materials based on $Ni_{2+x+y}Mn_{1-x}Ga_{1-y}$ alloys in which a giant magnetostrain is reached due to the shift in the martensitic transition temperature. A magnetic-field-controlled reversible shift in the temperature of the martensitic transformation in $Ni_{2+x}Mn_{1-x}Ga$ ($x = 0.16-0.19$) was observed in [48]. The shape-memory effect induced by a magnetic field and the related giant magnetostrains were investigated in polycrystalline samples of $Ni_{2+x-y}Mn_{1-x}Fe_yGa$ alloys [47]. Additions of iron were found to improve the mechanical properties of the $Ni_{2+x}Mn_{1-x}Ga$ alloys. To obtain a two-way shape-memory

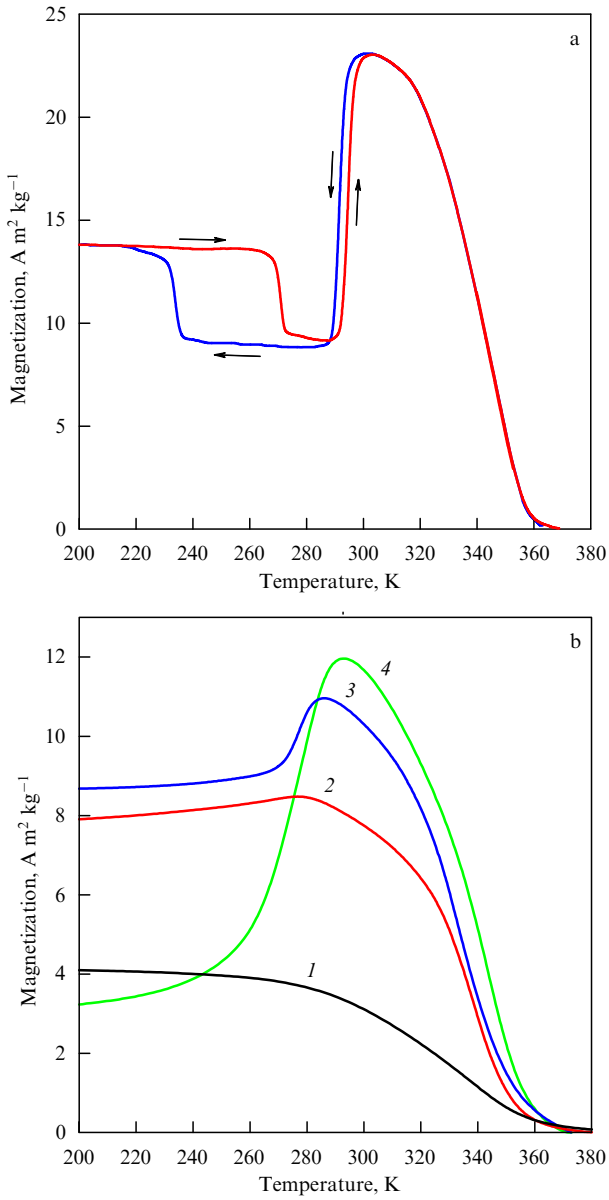


**Figure 3.** (a) Temperature dependences of the magnetization of a coarse-grained $Ni_{2.14}Mn_{0.81}Fe_{0.05}Ga$ alloy in the external magnetic field $H = 1$ T. (b) Temperature dependences of the magnetization of a nanocrystalline sample of the $Ni_{2.14}Mn_{0.81}Fe_{0.05}Ga$ alloy in the external magnetic field $H = 1$ T after annealing at various temperatures: (*1*) 623, (*2*) 673, (*3*) 773, and (*4*) 1073 K [41].

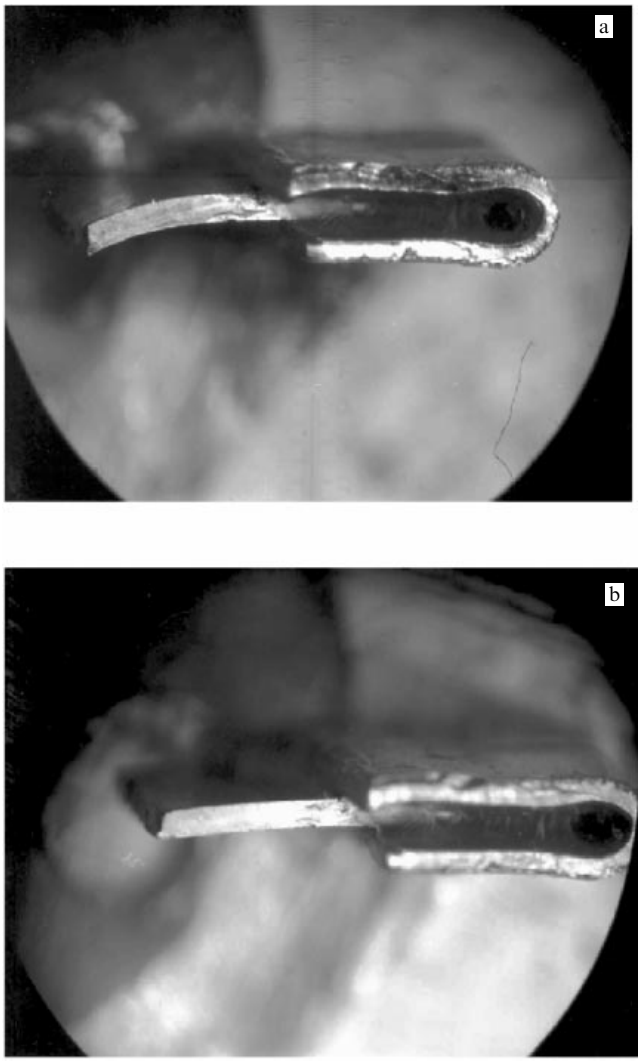


**Figure 4.** Photographs of a sample used in the experiments on the magnetically controlled shape-memory effect: (a) the magnetic field is switched on and (b) switched off [47].

effect, samples in the form of plates were 'trained' by thermocycling under a load. The training led to an increase in the limiting bending deformation from 2% for the untrained sample to 4.5% in samples subjected to multiple thermocycling. A shape-memory effect caused by the shift of the martensitic-transformation temperature by a magnetic field was observed in a trained platelet of the $Ni_{2.15}Mn_{0.81}Fe_{0.04}Ga$ alloy with $T_m \sim 313$ K. The experiment was conducted as follows. A plate, which was bent in the martensitic state, was placed at room temperature into the magnetic field $H = 10$ T. Then, the plate was heated in a field to $T = 315$ K and held at this temperature. Under these conditions, the bending deformation was $\sim 3\%$. After the magnetic field was switched off, the plate passed into the austenitic state and became completely unbent (Fig. 4). Thus, the bending deformation $\Delta e = 3\%$ was induced by the magnetic field $H = 10$ T.

The next step in the way of increasing the efficiency of controlling the dimensions and shape of the sample due to the shift of the martensitic transformation temperature was done in [50], where it was shown that with Ni substituted by Co in the Ni(Co)MnIn alloy, the transition of austenite into martensite is accompanied by the transition from the ferromagnetic state with a large saturation magnetization into a supposedly antiferromagnetic state with a zero spontaneous magnetization. Because the extent of the magnetic field effect on the structural transition temperature $T_m$ is determined by the difference in the magnetizations of the high-temperature and low-temperature phases, the application of a magnetic field of 7 T decreased $T_m$ by $\sim 30$ K. Because the temperature hysteresis of the martensitic transformation in this alloy is $\sim 8$ K, the reversible structural transition can be induced by a magnetic field that does not exceed 3 T. The experiments show that to obtain a 3% strain caused by the shift of the martensitic transformation temperature in a single-crystal sample, it suffices to apply a magnetic field equal to $\sim 4$ T.

Another mechanism of obtaining giant magnetostrains is the reorientation of martensitic variants by a magnetic field. This mechanism was suggested in [51] and realized for the first time in [1], where a strain of 0.2% induced by a magnetic field of 0.8 T in a single crystal of the $Ni_2MnGa$ Heusler alloy with the martensitic transformation temperature $T_m \sim 276$ K was reported. Later, 6% strains in the martensitic phase of single-crystals with a five-layer modulation were obtained [52]. Also reported was the occurrence of an irreversible 9% deformation in a single crystal with a seven-layer modulation [53]. An analysis of the dynamics of motion of martensitic variants under the effect of an ac magnetic field shows [54] that the response of the system to an external action can be observed up to the frequencies about 2 kHz.

From the standpoint of practical applications, the above-considered methods for obtaining giant magnetostrains in ferromagnets with a shape-memory effect have both advantages and drawbacks. For example, the advantages of producing magnetostrains due to the shift in the martensitic-transition temperature are the possibility of using inexpensive polycrystals, the universality of the deformation mode (linear deformations, bending, twisting), and the possibility of controlling deformations in actuators on a micron and submicron level. The shortcomings of this method are a relatively narrow range of working temperatures and the necessity in strong magnetic fields (about 10 T). We note, however, that recently observed results [50] give confidence that these drawbacks can be overcome.

### 3.2 The giant magnetocaloric effect in the magnetostructural transition

The problem of the investigation of the magnetocaloric effect in materials with a magnetostructural transition has been considered in numerous works. The greatest attention is paid to the alloys based on Gd(SiGe), (MnFe)(PAs), and La-Fe-Si [55]. The giant magnetocaloric effect observed in these alloys is due to the magnetostructural transition. It occurs at a temperature that is determined by the composition and can be close to room temperature. Such a possibility opens prospects for creating refrigerators working at room temperature for wide applications in industry and in private life. Of special interest are Heusler alloys, because they are ecological and do not contain poisonous or expensive rare-earth metals.

In Ni-Mn-Ga alloys with a coupled magnetostructural transition, the magnetocaloric effect has been studied in most detail in the case of the alloy of composition $Ni_{2.19}Mn_{0.81}Ga$ [56–59]. For this alloy, direct measurements of the adiabatic variation of the temperature upon the application of a magnetic field have been performed [58, 59], apart from the determination of the magnetocaloric effect from the results of the most common method — measurements of isothermal magnetization curves. The experimental $\Delta S(T)$ dependences determined from direct measurements are shown in Fig. 5. The curves have two sharp peaks at the temperatures 338 K and 344 K. In a magnetic field of 2.6 T, the greatest change in the entropy is 9 J kg$^{-1}$ K$^{-1}$ when the field is switched on at 338 K and 11 J kg$^{-1}$ K$^{-1}$ when the field is switched off at 344 K. The values of the magnetocaloric effect obtained (10 J kg$^{-1}$ K$^{-1}$) are close to the best values observed at room temperature for other known materials with the giant magnetocaloric effect [55]. The results of calculations based on the theory described in [57, 60, 61] give curves that agree well with the experimental results (see Fig. 5).

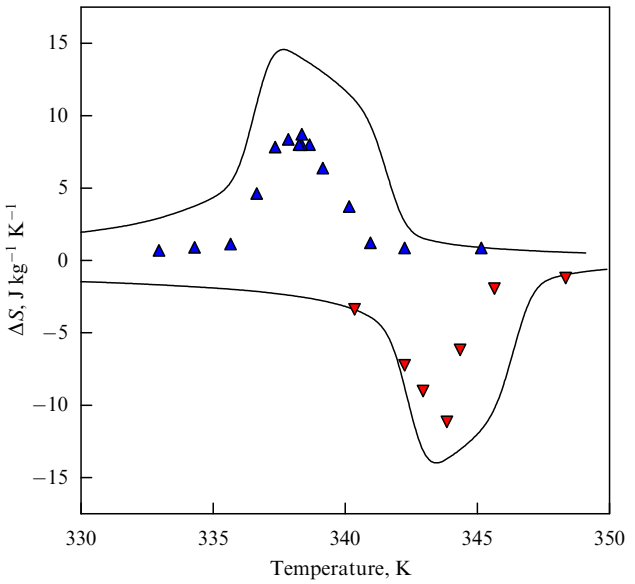


**Figure 5.** Direct measurements of the magnetocaloric effect in the $Ni_{2.19}Mn_{0.81}Ga$ alloy in the field 2.6 T. Symbols, experimental data points; solid curves, theory [59].

The giant magnetocaloric effect was observed not only in Ni-Mn-Ga alloys but also in Ni-Mn-Sn alloys [62]. We note that in the latter, the difference $\Delta S$ is positive. This is because the structural transition occurs from the austenitic ferromagnetic phase to the martensitic phase with a dominating antiferromagnetic exchange.

## 4. Applied capabilities of functional materials based on ferromagnetic alloys with the shape-memory effect

The discovery of the effect of giant strains caused by a rearrangement of martensitic variants in Ni-Mn-Ga single crystals under the action of a magnetic field [1] has attracted great attention to this problem. Only a few years later, commercial samples of actuators based on this material appeared on the market [63]. The results of ten years of work on the improvement of the extremely attainable parameters of the Ni-Mn-Ga alloys are as follows: the maximum limiting strains (compression – tension) up to 9.5% [53]; the recovery stress 2 MPa [52]; and the minimum response time 150 μs [54]. Commercial actuators produced by Adaptamat, Inc. (patents [64, 65]) ensure the following characteristics: the displacement of the actuating element up to 5 mm; frequency up to 1000 Hz; and the force up to 1000 N [63]. This technology is expensive and complex because of the necessity of using perfect single crystals; however, we cannot deny its potential, e.g., in the technology of hydroacoustic transducers.

It is obvious that the applied potential of the new materials is by no means exhausted by this application. Of great interest is the possibility of controlling the shape and dimensions of ferromagnets having the shape-memory effect by using a magnetically induced martensitic transformation [47, 48]. In the case of this mechanism, the actuating element (preliminarily trained for a two-way shape-memory effect) can change its shape under the effect of a magnetic field at a constant temperature in an arbitrary manner, i.e., can be bent, twisted, stretched, etc. These properties can find

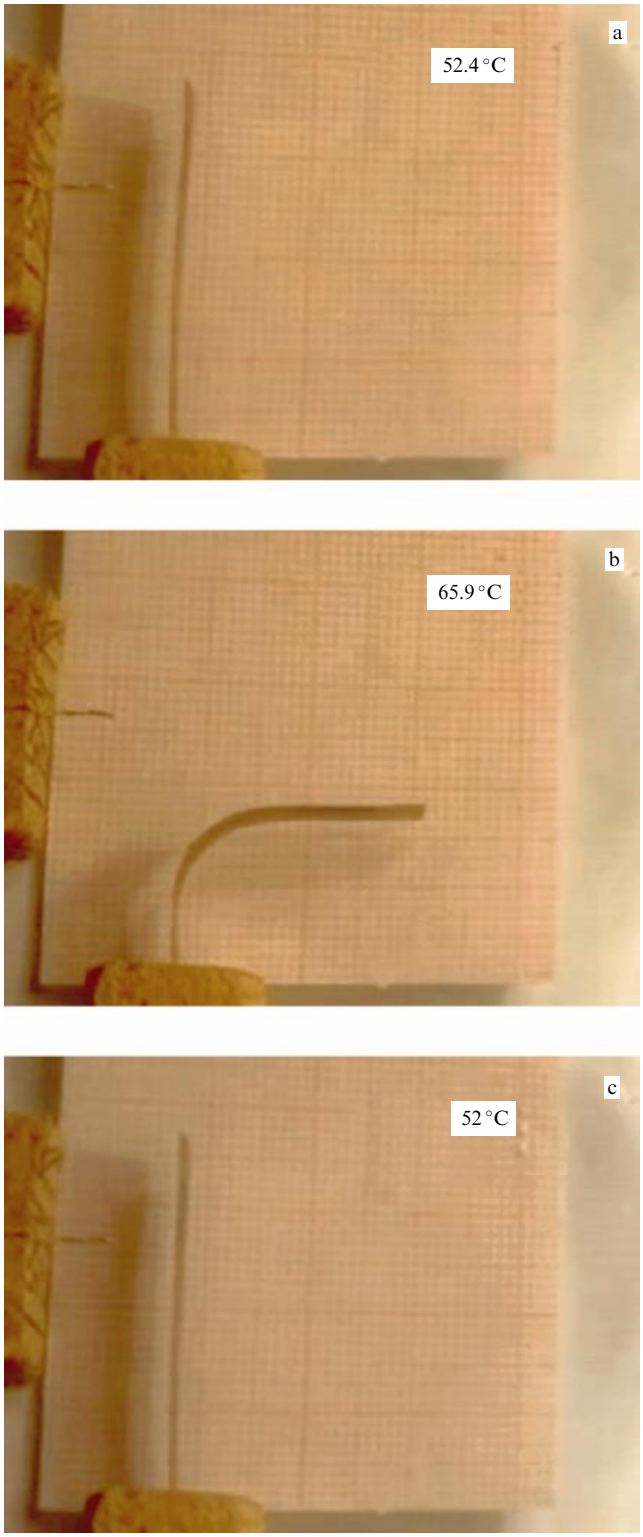


**Figure 6.** Variation in the shape of a bimetallic composite based on a shape-memory alloy: (a) in the low-temperature phase; (b) upon heating to above the martensitic transformation temperature; and (c) upon cooling to the low-temperature phase.

application in electronics, micro- and nanomechanics, and medicine.

The active elements of ferromagnets with the shape-memory effect have the property of changing their magnetic susceptibility upon the martensitic transformation and, consequently, upon pseudoplastic deformation. In devices similar to that described in [66], the magnetic state of the actuator itself serves as both the cause and the indicator of its mechanical state. Consequently, such a device combines the functional opportunities of a sensor and an actuator.

Recently, a new principle for creating reversible bending strains was suggested based on the use of layered composites consisting of ferromagnetic or nonferromagnetic materials with a shape-memory effect. This principle is analogous to the action of a bimetallic or a bimagnetostrictive plate, but the limiting reversible bending strains can in principle be greater by 1 – 3 orders of magnitude. Figure 6 shows the prototype of a composite whose bending is controlled by heating.

**Acknowledgments.** This work was supported in part by the Russian Foundation for Basic Research (project nos 04-02-81058-Bel, 05-02-19935-YaF, 05-0850341, 06-02-16266, and 06-02-16984); grants from the President of the Russian Federation (nos NSh-8269.2006.2, MK-5658.2006.2); a grant from the Ministry of Education of the Russian Federation and CRDF Y2-P-05-19; and a grant from the Ministry of Economic Development of the Chelyabinsk region.

## References

1. Ullakko K et al. *Appl. Phys. Lett.* **69** 1966 (1996)
2. Vasil'ev A N et al. *Usp. Fiz. Nauk* **173** 577 (2003) [*Phys. Usp.* **46** 559 (2003)]
3. Fradkin M A *Phys. Rev. B* **50** 16326 (1994)
4. Izyumov Yu A, Syromyatnikov V N *Fazovye Perekhody i Simmetriya Kristallov* (Phase Transitions and Crystal Symmetry) (Moscow: Nauka, 1984) [Translated into English (Dordrecht: Kluwer Acad. Publ., 1990)]
5. Krumhansl J A, Gooding R J *Phys. Rev. B* **39** 3047 (1989)
6. Gooding R J, Krumhansl J A *Phys. Rev. B* **38** 1695 (1988)
7. Buchel'nikov V D et al. *Zh. Eksp. Teor. Fiz.* **119** 1166 (2001) [*JETP* **92** 1010 (2001)]
8. Buchelnikov V D et al. *J. Magn. Magn. Mater.* **290 – 291** 854 (2005)
9. Tickle R, James R D *J. Magn. Magn. Mater.* **195** 627 (1999)
10. Shanina B D et al. *J. Magn. Magn. Mater.* **237** 309 (2001)
11. Buchelnikov V et al. *Int. J. Appl. Electromagn. Mech.* **12** 19 (2000)
12. Buchel'nikov V D et al. *Zh. Eksp. Teor. Fiz.* **119** 1176 (2001) [*JETP* **92** 1019 (2001)]
13. Zayak A T, Buchelnikov V D, Entel P *Phase Trans.* **75** 243 (2002)
14. Khovaylo V V et al. *Phys. Rev. B* **72** 224408 (2005)
15. Vasil'ev A N et al. *Phys. Rev. B* **59** 1113 (1999)
16. Khovailo V V et al. *J. Phys.: Condens. Matter* **13** 9655 (2001)
17. Buchelnikov V D, Khovailo V V, Takagi T *J. Magn. Magn. Mater.* **300** e459 (2006)
18. Chernenko V A *Scripta Mater.* **40** 523 (1999)
19. Webster P J et al. *Philos. Mag. B* **49** 295 (1984)
20. Watson R E, Weinert M, in *Solid State Physics* Vol. 56 (Eds H Ehrenreich, F Spaepen) (New York: Academic Press, 2001) p. 1
21. Lanska N et al. *J. Appl. Phys.* **95** 8074 (2004)
22. Jiang C et al. *Acta Mater.* **52** 2779 (2004)
23. Oikawa K et al. *Mater. Trans.* **42** 2472 (2001)
24. Oikawa K et al. *Appl. Phys. Lett.* **79** 3290 (2001)
25. Oikawa K et al. *Appl. Phys. Lett.* **81** 5201 (2002)
26. Oikawa K et al. *Mater. Trans.* **43** 2360 (2002)
27. Sutou Y et al. *Appl. Phys. Lett.* **85** 4358 (2004)
28. Krenke T et al. *Phys. Rev. B* **72** 014412 (2005)
29. MacLaren J M *J. Appl. Phys.* **91** 7801 (2002)
30. Enkovaara J et al. *Phys. Rev. B* **67** 212405 (2003)
31. Khovailo V V et al. *Phys. Rev. B* **70** 174413 (2004)
32. Li J Q et al. *Solid State Commun.* **126** 323 (2003)
33. Murakami Y et al. *Appl. Phys. Lett.* **82** 3695 (2003)
34. Oikawa K et al. *J. Magn. Magn. Mater.* **272 – 276** 2043 (2004)
35. Sutou Y et al. *Appl. Phys. Lett.* **84** 1275 (2004)
36. Zheng H X et al. *J. Alloys Comp.* **385** 144 (2004)
37. Zheludev A et al. *Phys. Rev. B* **54** 15045 (1996)

38. Velikokhatnyi O I, Naumov I I *Fiz. Tverd. Tela* **41** 684 (1999) [*Phys. Solid State* **41** 617 (1999)]
39. Gusev A I, Rempel' A A *Nanokristallicheskie Materialy* (Nanocrystalline Materials) (Moscow: Fizmatlit, 2000); see also *Nanocrystalline Materials* (Cambridge: Cambridge Intern. Sci. Publ., 2004)
40. Imashev R N et al. *Dokl. Ross. Akad. Nauk* **400** 333 (2005) [*Dokl. Phys.* **50** 28 (2005)]
41. Imashev R N et al. *J. Phys.*: *Condens. Matter* **17** 2129 (2005)
42. Imashev R N et al. *Fiz. Tverd. Tela* **47** 536 (2005) [*Phys. Solid State* **47** 556 (2005)]
43. Sharipov I Z, Mulyukov R R, Mulyukov Kh Ya *Fiz. Met. Metalloved.* **95** (1) 47 (2003) [*Phys. Met. Metallogr.* **95** 42 (2003)]
44. Kim K W et al. *J. Magn. Magn. Mater.* **272 – 276** 1176 (2004)
45. Kim K W et al. *J. Korean Phys. Soc.* **45** 28 (2004)
46. Krivoglaz M A, Sadovskii V D *Fiz. Met. Metalloved.* **18** 502 (1964)
47. Cherechukin A A et al. *Phys. Lett. A* **291** 175 (2001)
48. Dikshtein I E et al. *Pis'ma Zh. Eksp. Teor. Fiz.* **72** 536 (2000) [*JETP Lett.* **72** 373 (2000)]
49. Takagi T et al. *Int. J. Appl. Electromagn. Mech.* **16** 173 (2002)
50. Kainuma R et al. *Nature* **439** 957 (2006)
51. Ullakko K *J. Mater. Eng. Perform.* **5** 405 (1996)
52. Murray S J et al. *Appl. Phys. Lett.* **77** 886 (2000)
53. Sozinov A et al. *Appl. Phys. Lett.* **80** 1746 (2002)
54. Marioni M A, O'Handley R C, Allen S M *Appl. Phys. Lett.* **83** 3966 (2003)
55. Gschneidner K A (Jr), Pecharsky V K, Tsokol A O *Rep. Prog. Phys.* **68** 1479 (2005)
56. Pareti L et al. *Eur. Phys. J. B* **32** 303 (2003)
57. Aliev A et al. *J. Magn. Magn. Mater.* **272 – 276** 2040 (2004)
58. Aliev A M et al., in *Proc. of the First IIR Intern. Conf. on Magnetic Refrigeration at Room Temperature, Montreux, Switzerland, 27 – 30 September 2005*, p. 135
59. Buchelnikov V D et al. *Int. J. Appl. Electromagn. Mech.* (in press)
60. Buchelnikov V D, Bosko S I *J. Magn. Magn. Mater.* **258 – 259** 497 (2003)
61. Bosko S I, Buchelnikov V D, Takagi T *J. Magn. Magn. Mater.* **272 – 276** 2102 (2004)
62. Krenke T et al. *Nature Mater.* **4** 450 (2005)
63. AdaptaMat, http://www.adaptamat.com/
64. O'Handley R C, Ullakko K M, US Patent No. 5958154 (September 28, 1999)
65. Ullakko K M, US Patent No. 6157101 (December 5, 2000)
66. Kohl M et al. *Sensors Actuators A* **114** 445 (2004)